



# 1 Feasibility of robust estimates of ozone production rates 2 using satellite observations

3

4 Amir H. Souri<sup>1,2\*</sup>, Gonzalo González Abad<sup>3</sup>, Glenn M. Wolfe<sup>1</sup>, Tijn Verhoelst<sup>4</sup>, Corinne Vigouroux<sup>4</sup>,  
5 Gaia Pinardi<sup>4</sup>, Steven Compernelle<sup>4</sup>, Bavo Langerock<sup>4</sup>, Bryan N. Duncan<sup>1</sup>, Matthew S. Johnson<sup>5</sup>

6

7 <sup>1</sup>Atmospheric Chemistry and Dynamics Laboratory, NASA Goddard Space Flight Center, Greenbelt, MD,  
8 USA

9 <sup>2</sup>GESTAR II, Morgan State University, Baltimore, MD, USA

10 <sup>3</sup>Atomic and Molecular Physics (AMP) Division, Center for Astrophysics | Harvard & Smithsonian,  
11 Cambridge, MA, USA

12 <sup>4</sup>Royal Belgian Institute for Space Aeronomy (BIRA-IASB), Ringlaan 3, 1180 Uccle, Belgium

13 <sup>5</sup>Earth Science Division, NASA Ames Research Center, Moffett Field, CA, USA

14 \* Corresponding author: [a.souri@nasa.gov](mailto:a.souri@nasa.gov)

15

## 16 Abstract.

17 Ozone pollution is secondarily produced through a complex, non-linear chemical process. Our  
18 understanding of the spatiotemporal variations in photochemically produced ozone (i.e., PO<sub>3</sub>) is limited to  
19 sparse aircraft campaigns and chemical transport models, which often carry significant biases. Hence, we  
20 present a novel satellite-derived PO<sub>3</sub> product informed by bias-corrected TROPOMI HCHO, NO<sub>2</sub>, surface  
21 albedo data, and various models. These data are integrated into a parameterization that relies on HCHO,  
22 NO<sub>2</sub>, HCHO/NO<sub>2</sub>, jNO<sub>2</sub>, and jO<sup>1</sup>D. Despite its simplicity, it can reproduce ~90% of the variance in  
23 observationally constrained PO<sub>3</sub> with minimal biases in moderately to highly polluted regions. We map PO<sub>3</sub>  
24 across various regions in July 2019 at a 0.1°×0.1° spatial resolution, revealing accelerated values (>8  
25 ppbv/hr) in numerous cities throughout Asia and the Middle East, resulting from the elevated ozone  
26 precursors and enhanced photochemistry. In Europe and the United States, such high levels are only  
27 detected over Benelux, Los Angeles, and New York City. PO<sub>3</sub> maxima are seen in various seasons, attributed  
28 to changes in photolysis rates, non-linear ozone chemistry, and fluctuations in HCHO and NO<sub>2</sub>. Satellite  
29 errors result in moderate errors (40-60%) of PO<sub>3</sub> estimates over cities on a monthly average, while these  
30 errors exceed 100% in clean areas and under low light conditions. Using the current algorithm, we have  
31 demonstrated that satellite data can provide valuable information for robust PO<sub>3</sub> estimation. This capability  
32 expands future research through the application of data to address significant scientific questions about the  
33 locally-produced PO<sub>3</sub> hotspots, seasonality, and long-term trends.

## 34 1. Introduction

35 Tropospheric ozone (O<sub>3</sub>) is a secondary pollutant formed through complex photochemical reactions  
36 involving various precursors, including nitrogen oxides (NO<sub>x</sub> = NO + NO<sub>2</sub>), volatile organic compounds  
37 (VOCs), aerosols, and halogens (Kleinman et al., 2002, Simpson et al., 2015; Li et al., 2019). Ozone not  
38 only poses significant risks to human health and agricultural productivity but also influences the radiation



39 budget, thereby affecting the climate. To mitigate the problem of elevated locally-produced ozone, it is  
40 crucial to understand the spatiotemporal variability in ozone production rates ( $PO_3$ ), defined as the number  
41 of ozone molecules generated through secondary chemical pathways in the atmosphere. Comprehensive  
42 studies of ozone chemistry, informed by observations, are typically confined to observationally-rich air  
43 quality campaigns (e.g., Cazorla et al., 2012; Ren et al., 2013; Mazzuca et al., 2016; Souri et al., 2020a;  
44 Schroeder et al., 2020; Brune et al., 2022; Wolfe et al., 2022; Souri et al., 2023), which are sparse in time  
45 and space.

46 Significant advancements have been achieved in using various measurable ozone indicators to  
47 simplify the non-linear relationship between  $PO_3$  and  $NO_x$  and VOCs into linear forms (Sillman and He,  
48 2002). These forms include  $NO_x$ -sensitive (where  $PO_3$  is sensitive to  $NO_x$ ), VOC-sensitive (where  $PO_3$  is  
49 sensitive to VOCs), and the transitional regimes (where  $PO_3$  is sensitive to both  $NO_x$  and VOCs). Among  
50 the numerous proposed indicators, the ratio of formaldehyde (HCHO) to nitrogen dioxide ( $NO_2$ ) (known as  
51 FNR) has gained popularity (Tonnesen and Dennis, 2000a,b), despite its less effective performance  
52 compared to the  $H_2O_2/HNO_3$  ratio in fully explaining the  $HO_x$ - $RO_x$  cycle (Sillman and He, 2002; Souri et  
53 al., 2023). The preference for FNR stems from the fact that both quantities can be informed by UV-Vis  
54 radiance data, such as those provided by the Ozone Monitoring Instrument (OMI) and the TROPospheric  
55 Monitoring Instrument (TROPOMI) (Martin et al., 2005; Duncan et al., 2010; Choi et al., 2012; Choi and  
56 Souri, 2015a, b; Jin and Holloway, 2015; Jin et al., 2017; Schroeder et al., 2017; Souri et al., 2017; Jeon et  
57 al., 2018; Tao et al., 2022). Several limitations associated with the application of satellite-based FNR have  
58 been identified such as i) the inherent limitation of understanding the radical termination in the  $RO_x$ - $HO_x$   
59 cycle (Souri et al., 2020a; Souri et al., 2023), ii) the challenges associated with converting the column  
60 vertical density to the near-surface concentrations (Jin et al., 2017; Schroeder et al., 2017; Souri et al.,  
61 2023), iii) spatial representativity associated with large satellite pixels (Souri et al., 2020a, 2023; Johnson  
62 et al., 2023), and iv) the retrieval errors (Souri et al., 2023; Johnson et al., 2023). Souri et al. (2023)  
63 concluded that the retrieval errors make up the largest portion of total errors associated with FNR. These  
64 errors are becoming smaller with better sensor designs, retrieval algorithms, and calibration over time.

65 While the characterization of ozone regimes offers valuable insights for regulators to prioritize  
66 effective emission control strategies, it does not provide information about the magnitude of  $PO_3$  or the  
67 absolute quantities of  $PO_3$  derivatives relative to its precursors. Consequently, chemical transport models  
68 under various emission scenarios are typically employed (e.g., Pan et al., 2019). These models allow for  
69 the execution of process-based scenarios to elucidate the response of  $PO_3$  to different emissions and can  
70 simulate four-dimensional  $PO_3$  data. However, the results of these simulations are based on various  
71 assumptions and inputs, which carry significant uncertainties. Therefore, it is essential to optimize some of  
72 the models' prognostic inputs using observations through inverse modeling/data assimilation. The primary  
73 advantage of inverse modeling/data assimilation using satellite observations is its ability to account for  
74 satellite errors and eliminate the influence of the a priori profile, thereby carrying only radiance information  
75 into the emission estimation. Numerous studies have utilized satellite observations to constrain  $NO_x$  and  
76 VOC emissions for various applications (e.g., Stavrou et al., 2016; Souri et al., 2016; Miyazaki et al.,  
77 2017; Souri et al., 2017; Souri et al., 2020b; Souri et al., 2021; Choi et al., 2022; DiMaria et al., 2023).  
78 Souri et al. (2020b) made an early attempt to simultaneously optimize both  $NO_x$  and VOC emissions over  
79 East Asia for a more accurate representation of  $PO_3$ . Their joint-inversion was able to account for the  
80 intertwined relationship between HCHO- $NO_x$  and  $NO_2$ -VOC. However, the execution of chemical transport  
81 models optimized by multiple satellite observations remains prohibitively expensive, particularly for high-  
82 resolution domains demanded by regulatory agencies.

83 Data-driven methods for estimating  $PO_3$  have emerged as a more cost-effective alternative to  
84 physics-based methods. While using constrained chemical transport models provides a relatively robust  
85 framework grounded in some explicit governing equations, they require extensive computation resources  
86 and expertise. Conversely, data-driven algorithms make use of large datasets to identify patterns and make  
87 predictions with much reduced computational expenses. However, it is important to recognize that data-



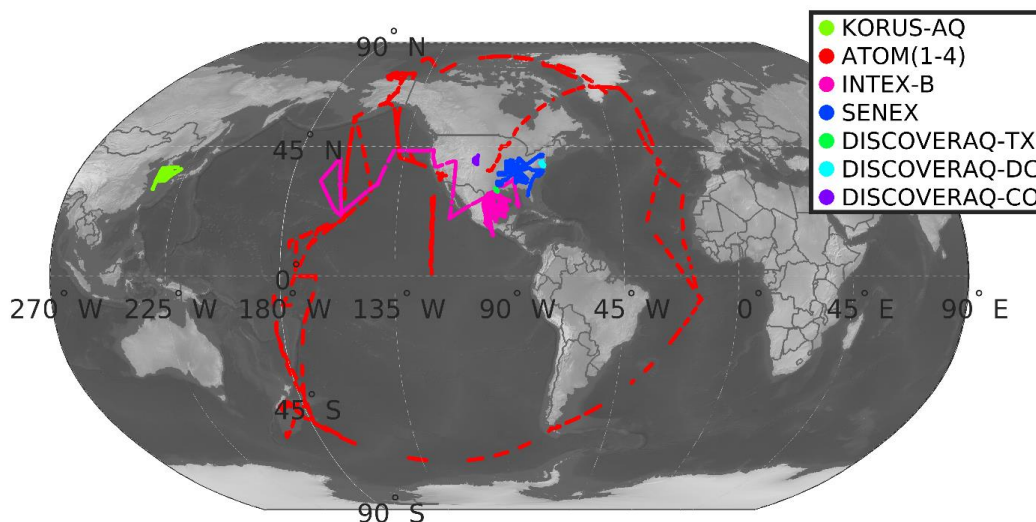
88 driven algorithms lack the ability to provide solid physical interpretability and generalizability. Despite this  
89 fundamental limitation, they are sensible tools for applications where rapid analysis over a wide spatial  
90 coverage is prioritized. Data-driven parameterizations for several components of atmospheric chemistry  
91 such as OH (Anderson et al., 2022) and dry deposition (Silva et al., 2019) have been crafted for this reason.  
92 However, to our best knowledge, Chatfield et al. (2010) and Souri et al. (2023) are the only studies that  
93 attempted to empirically parameterize  $\text{PO}_3$  using the information of HCHO and  $\text{NO}_2$  mixing ratios. Inspired  
94 by those works, we developed a novel product using TROPOMI observations in conjunction with  
95 atmospheric models to provide  $\text{PO}_3$  and associated errors within the planetary boundary layer (PBL) across  
96 the globe. This enabled us to map  $\text{PO}_3$  across various regions at fine scales (i.e.,  $0.1 \times 0.1$  degrees) for the  
97 first time.

## 98 **2. Data**

### 99 **2.1. Aircraft**

100 To study  $\text{PO}_3$ , we use various aircraft observations from several NASA and NOAA atmospheric  
101 composition campaigns. We have selected three sets of aircraft campaigns for the purpose of  $\text{PO}_3$   
102 estimation, targeting: i) urban/suburban air quality, including Deriving Information on Surface Conditions  
103 from Column and Vertically Resolved Observations Relevant to Air Quality (DISCOVER-AQ) Baltimore-  
104 Washington (2011), DISCOVER-AQ Houston-Texas (2013), DISCOVER-AQ Colorado (2014), and the  
105 Korea United States Air Quality Study (KORUS-AQ) (2016) (Crawford et al., 2021); ii) remote areas  
106 including Atmospheric Tomography Mission (ATOM) (Thompson et al., 2022) and Intercontinental  
107 Chemical Transport Experiment (INTEX) phase B (Singh et al., 2009); iii) a mixture of isoprene-rich  
108 environment and large emitters, including SENEX (Southeast Nexus) (Warneke et al., 2016). Figure 1  
109 shows the location of these campaigns. Inspired by the study of Miller and Brune (2022), we list their  
110 “when, where, why” characteristics in Table S1.

111 For aircraft campaigns targeting polluted areas, including DISCOVERs, KORUS-AQ, SENEX,  
112 and SEAC4RS, we use 10-sec merged data, whereas, for other measurements taken in relatively remote  
113 areas, such as INTEX-B and ATOMs, we used 30-sec merged data. A more detailed description of the  
114 measurements is provided in Section 3.2. We exclude times with no measurements of NO,  $\text{NO}_2$ , or HCHO.  
115 The concentrations of OH and  $\text{HO}_2$  were only measured during INTEX-B, ATOMs, and KORUS-AQ.  
116 Likewise, we void any data points lacking either  $\text{HO}_2$  or OH measurements. There are frequent gaps in  
117 some measurements, especially for VOCs, because of instrument issues or measurement techniques.  
118 Following Souri et al. (2020a), Miller and Brune (2020), Souri et al. (2023), and Bottorff et al. (2023), we  
119 fill the gaps in measurements using a linear interpolation method with no extrapolation allowed beyond 15  
120 minutes. We drop any remaining gaps from the analysis. To better capture the rapid fluctuation of VOCs,  
121 we pick the PTR-TOF-MS instrument with high temporal resolution over the whole air sampler (WAS)  
122 when both instruments have measured the same quantity. Regarding the INTEX-B campaign, we drop  
123 isoprene observation due to infrequent samples downgrading the performance of our box model.



124

125 **Figure 1.** The location of seven different atmospheric composition aircraft campaigns used in this study.

126 **2.2. TROPOMI NO<sub>2</sub> and HCHO**

127 We use the recently reprocessed daily level-2 (L2) TROPOMI tropospheric NO<sub>2</sub> and total HCHO  
 128 columns derived from UV-visible radiances onboard the European Space Agency's (ESA's) Sentinel-5  
 129 Precursor (S5P) spacecraft (~328-496 nm) (Veeffkind et al., 2012, De Smedt et al. 2021; van Geffen et al.,  
 130 2022). This sensor has been operational since May 2018, providing global coverage of NO<sub>2</sub> and HCHO at  
 131 ~1:30 local standard time at the Equator. Since NO<sub>2</sub> and HCHO are optically thin absorbers in the UV-  
 132 Visible, meaning their concentrations do not substantially affect the sensitivity of the radiance to the optical  
 133 thickness of the absorber, the retrieval follows the conventional two-step algorithm involving spectral fitting  
 134 for Slant Column Density (SCD) retrieval and Air Mass Factor (AMF) calculations for SCD to Vertical  
 135 Column Density (VCD) conversion. The product has a spatial resolution of 7.2 km (5.6 km as of August  
 136 2019) by 3.6 km at nadir. To remove unfit measurements, we use the provided quality flag (*q\_value*) and  
 137 choose only those above 0.75 for NO<sub>2</sub> and 0.5 for HCHO. As the L2 product does not come in a regular  
 138 grid, we use a mass-conserved regridding technique based on barycentric linear interpolation to map out  
 139 the data onto a 0.1°×0.1° regular grid.

140 van Geffen et al. (2022) demonstrated that the reprocessed TROPOMI tropospheric NO<sub>2</sub> columns  
 141 exhibit a good level of correspondence with those obtained from ground-based MAX-DOAS sky  
 142 spectrometers, with a correlation of 0.88 and a median bias of -23%, improving on the older product  
 143 versions which were biased low by about 30% with respect to ground-based measurements at polluted sites  
 144 (Verhoelst et al., 2021). More information about new modifications and their impacts on the retrieval can  
 145 be found in van Geffen et al. (2022).

146 The studies of Vigouroux et al. (2020) and De Smedt et al. (2021) validated the reprocessed  
 147 monthly-mean TROPOMI HCHO columns against FTIR and MAX-DOAS observations and found a good  
 148 correlation above 0.8 with a negative bias of 20-30% for polluted sites. The bias tends to be slightly positive  
 149 or neutral over clean sites.

150 **2.2.1. Error characterization of TROPOMI NO<sub>2</sub> and HCHO using sky-radiance retrievals**

151 To propagate TROPOMI retrieval errors to the PO<sub>3</sub> product and to remove potential biases, we  
 152 assume three origins for errors: i) random errors resulting from instrument noise, ii) a fixed additive



153 component that is magnitude-independent, and iii) unresolved systematic biases that are multiplicative and  
 154 irreducible by oversampling. The first component is derived from the column precision variable provided  
 155 along with the L2 product. In the spatial domain, we interpolate the squares of this error the same of way  
 156 we map the irregular L2 pixels into the  $0.1^\circ \times 0.1^\circ$  regular grid. Moreover, to mitigate this error, its squares  
 157 are averaged for over a month. Two other errors are determined by comparing FTIR (for HCHO) and MAX-  
 158 DOAS (for tropospheric  $\text{NO}_2$ ) with TROPOMI data (Section 4.3.3). Detailed explanation of how these  
 159 datasets are paired can be found in Vigouroux et al. (2020) and Verhoelst et al. (2021). Both datasets cover  
 160 the period of 2018-2023.

161 To achieve an optimal linear fit ( $y = ax + b + \varepsilon$ ) between the paired observations, we follow a  
 162 Monte-Carlo Chi-squares minimization such that  $\chi^2 = \sum \frac{[y-f(x_i,a,b)]^2}{\sigma_y^2 + a^2 \sigma_x^2}$  is minimized.  $\sigma_y^2$  and  $\sigma_x^2$  are the  
 163 variances of  $y$  (TROPOMI) and  $x$  (the benchmark), respectively. In terms of TROPOMI  $\text{NO}_2$  and HCHO,  
 164 the errors are populated based on the L2 information. According to Verhoelst et al. (2021), a fixed error of  
 165 30% is assumed for MAX-DOAS  $\text{NO}_2$  observations whose values are above  $1.4 \text{ Pmolec/cm}^2$ . Because of  
 166 the detection limit of MAX-DOAS  $\text{NO}_2$ , we set errors for values below that threshold to  $1.4 \text{ Pmolec/cm}^2$ .  
 167 The FTIR retrieval errors described in Vigouroux et al. (2020) were used to populate the errors associated  
 168 with this benchmark. The minimization is performed 10000 times, each with a set of random perturbations  
 169 of  $x$  and  $y$  within their respective prescribed errors. This approach allows us to assess the robustness of the  
 170 estimates across the range of errors associated with each data point.

171 The offset (a uniform additive term) and the slope (multiplicative error) drawn from the ground  
 172 validation are used to correct the biases associated with TROPOMI via:

$$VCD_{bias-corrected} = \frac{VCD_{original} - offset}{slope} \quad (1)$$

173 Since there are errors associated with this adjustment resulting from instrument and representation errors,  
 174 we augment errors of the slope and offset to the total error and label them constant errors ( $e_{const}^2$ ) via:

$$e_{const}^2 = e_{offset}^2 + e_{slope}^2 \times VCD_{bias-corrected}^2 \quad (2)$$

175 where  $e_{offset}^2$  and  $e_{slope}^2$  are errors of offset and slope calculated from the linear regression. Ultimately, the  
 176 sum of all three errors constitutes the total errors given:

$$e^2 = e_{const}^2 + \frac{1}{m^2} \sum_{i=1}^m e_{random,i}^2 \quad (3)$$

177 where  $m$  is the number of samples for a given grid and timeframe and  $e_{random}$  is random errors.

### 178 2.3. TROPOMI Surface Albedo

179 To account for the effect of surface albedo on photolysis rates (Section 2.5), we use a newly  
 180 developed algorithm based on the directionally dependent Lambertian-equivalent reflectivity (DLER) UV  
 181 surface albedo climatology made from TROPOMI radiance (Tilstra et al., 2024). This new database  
 182 leverages 60 months of TROPOMI reprocessed radiance and is produced at the grid resolution of  
 183  $0.125^\circ \times 0.125^\circ$ . The product has outperformed traditional LER products such as OMI when both were  
 184 compared to MODIS surface BRDF results (Tilstra et al., 2024).

### 185 2.4. MERRA2-GMI

186 To convert vertical column densities of HCHO and  $\text{NO}_2$  from TROPOMI to their volume mixing  
 187 ratios in the PBL region, we use the MERRA2-GMI model ([5](https://acd-</a></p>
</div>
<div data-bbox=)





188 ext.gsfc.nasa.gov/Projects/GEOSCCM/MERRA2GMI/, last access: 10 Sep 2023). This model is a NASA's  
 189 Goddard Earth Observing System (GEOS) Chemistry-Climate Model (CCM) run spanning for the period  
 190 of 1980-2019, exploiting MERRA2 (Modern Era Retrospective analysis for Research and Applications) to  
 191 constrain meteorological fields (Orbe et al., 2017). The model uses the Global Modeling Initiative (GMI)  
 192 chemical mechanism (Duncan et al., 2007; Strahan et al., 2007), which involves over 120 species and 400  
 193 reactions. It has a resolution of approximately 0.625° longitude by 0.5° latitude with 72 vertical layers  
 194 stretching from the surface up to 0.1 hPa. Additional information about the configuration of this model can  
 195 be found in Strode et al. (2019).

## 196 2.5. TUV NCAR Photolysis Rates Look-up Table

197 To estimate photolysis rates of JNO<sub>2</sub> (NO<sub>2</sub>+hv) and JO<sup>1</sup>D (O<sub>3</sub>+hv), we use a comprehensive look-  
 198 up table provided by the F0AM model (Section 3.2) created for clear-sky conditions. This look-up table is  
 199 based on the calculation of more than 20,064 solar spectra over a wide range of SZA (0:5:90°), altitude  
 200 (0:1:15 km), overhead total ozone column (100:50:600 DU), and surface UV albedo (0:0.2:1) using  
 201 NCAR's Tropospheric Ultraviolet and Visible radiation model (TUV v5.2) and cross sections and quantum  
 202 yields from IUPAC and JPL (Wolfe et al., 2016). The L2 TROPOMI granule information populates SZA,  
 203 surface elevation, and surface UV albedo, while overhead total ozone columns are obtained from MERRA2-  
 204 GMI (Section 2.4) which is found to agree well with satellite observations (Souri et al., 2024). Any values  
 205 between these tables are bilinearly interpolated for a smoother result.

## 206 3. Methods

### 207 3.1. LASSO

208 Through the use of multi-linear regression models, it is possible to establish a simple but robust  
 209 relationship between multiple variables and a target. However, when dealing with a large number of  
 210 variables, there is a chance of introducing overfitting issues. This can lead to predictions that are either  
 211 overly optimistic or unrealistic for values outside of the training dataset. To avoid this, it is recommended  
 212 to simplify the model by removing variables that are loosely connected with the target or highly correlated  
 213 with others. This process is known as "model shrinkage" and can narrow down the number of possible  
 214 solutions (i.e., variance) at the cost of increasing the biases between the observed target and predictions.  
 215 Ideally, we want a model that minimizes the sum of the bias and the variance. To achieve this, we can use  
 216 LASSO (least absolute shrinkage and selection operator) (Tibshirani, 1996) consider a regression,

$$Y = X\beta + \alpha + \varepsilon \quad (4)$$

217 with response  $Y = (y_1, \dots, y_n)^T$ ,  $n \times p$  explanatory variables  $X$ , coefficients  $\beta = (\beta_1, \dots, \beta_p)^T$ , an intercept  $\alpha$ ,  
 218 and noise variables  $\varepsilon = (\varepsilon_1, \dots, \varepsilon_n)^T$ . We can label the regression model sparse when many of  $\beta$  values are  
 219 zero, and we can label it high dimensional when  $p \gg n$ . LASSO attempts to select variables such that the  
 220 following cost function is minimized:

$$(\hat{\alpha}, \hat{\beta}) = \underset{\alpha, \beta}{\operatorname{argmin}} \left\{ \|Y - X\beta - \alpha\|_2 + \lambda \sum_{i=1}^p |\beta_i| \right\} \quad (5)$$

221 The first term on the right side of Eq.5 minimizes the squares of the residuals, whereas the second term  
 222 reduces the sum of absolute value of coefficients resulting in a simpler model with fewer parameters.  
 223 Without the second term, the regression model becomes an ordinary least-squares estimation. The most  
 224 critical element here is  $\lambda$ , a non-negative regularization factor. A large  $\lambda$  results in more aggressive  
 225 regularization leading to more model shrinkage, whereas a small value preserves a high dimensional model.  
 226 To optimize this value, we discretize  $\lambda$  in 100 values between  $10^{-4}$  up to  $10^1$ , divide the training dataset into



227 10 folds, determine the average of cross-validated error prediction among all folds, and find  $\lambda$  that yields  
228 the smallest error. The final solution ensures a balanced model with respect to model parsimony and bias.  
229 All explanatory variables are standardized during the regularization procedure such that their mean becomes  
230 zero and their standard deviation one.

### 231 **3.2. Photochemical box modeling**

232 To produce training data sets for LASSO-based  $PO_3$  estimation, we use the Framework for 0-D  
233 Atmospheric Modeling (F0AM) v4 box model (Wolfe et al., 2016), constrained by a wide range of  
234 observations. These observations ensure that the model achieves a realistic range of values found in the  
235 atmosphere. We follow past setups which apply the Carbon Bond 6 (CB06, r2) chemical mechanism in  
236 F0AM (Souri et al., 2020a; Souri et al., 2023). The model is constrained by aircraft data, including  
237 meteorology, photolysis rates, and trace gas concentrations. The model configuration and observations used  
238 are listed in Table S2.

239 Once the model is initialized and held constant with respect to a wide range of constraining  
240 quantities, it runs at 30 minutes integration time cycling for five days to approach a steady-state  
241 environment. Several key compounds including OH,  $HO_2$ , HCHO, PAN, NO, and  $NO_2$  are initialized with  
242 aircraft observations but they are left free to cycle with incoming solar radiation variability. These  
243 compounds play a crucial role in validating the efficacy of model performance as well as the adequacy of  
244 observations used as constraints. In particular, allowing HCHO to vary freely enables us to assess whether  
245 our mechanism for VOC treatment, steady-state, and the number of measured VOCs suffice to reproduce  
246 its concentrations reasonably. Although the individual concentration of  $NO_2$  and NO are not constrained,  
247 we constrain total  $NO_x$  ( $NO+NO_2$ ). Not all aircraft campaigns measured all photolysis rates included in the  
248 chemical mechanism. We first initialize the photolysis rates included in CB06 using the look-up-tables  
249 described in Section 2.5. If any photolysis reaction rates in CB06 were measured, we replace the initial  
250 guess with the observed values. For those reactions with photolysis rates not been measured, we apply a  
251 scaling factor made of the average of the ratio of the observed J-values to the modeled J-values. This  
252 approach is a sensible choice for accounting for large particles such as clouds, as their extinction coefficient  
253 is somewhat non-selective in the UV-Vis range; however, applying a wavelength-independent scaling factor  
254 may introduce some biases for optically complex environments introduced by aerosols.

255 It is essential to acknowledge the inherent limitations of a box model in our research. The model  
256 does not consider the diverse physical loss pathways that trace gases may undergo, including deposition  
257 and transport. As a result, we have simplified the physical loss by employing a first-order dilution rate set  
258 to  $1/86400\text{ s}^{-1}$ , equivalent to a lifetime of 24 hours. This approach ensures that unconstrained trace gases  
259 that take longer to break down do not accumulate over time. Exact knowledge of dilution factors requires  
260 knowing molecular and turbulent diffusion, entrainment and detrainment, and deposition rates, all of which  
261 are unknown at the micro-scale level of aircraft observations. Nonetheless, studies of Brune et al. (2022)  
262 and Souri et al. (2023) showed that  $HO_2$ , OH,  $NO_x$ , and HCHO are relatively immune to the choice of the  
263 dilution factor, whereas  $RO_2$  mixing ratios can depart introducing some biases in  $PO_3$  estimates.

264 We determine simulated  $PO_3$  by:

$$265 \quad PO_3 = FO_3 - LO_3 \quad (6)$$

266 where  $LO_3$  is all possible chemical loss pathways of ozone (negative stoichiometric multiplier matrix) and  
267  $FO_3$  is all possible chemical pathways producing ozone molecules (positive stoichiometric multiplier  
268 matrix). This calculation is theoretically equivalent to a value obtained from a chemical solver quantifying  
269 the number of ozone molecules produced/lost for each model timestep. The adoption of Eq.3 facilitates the  
270 direct comparison of  $PO_3$  estimations with those derived from other models, including CTM-based results  
271 (see Figure 10 in Souri et al., 2021). Furthermore, it allows for a seamless integration of these estimates  
into Lagrangian transport models for ozone forecasting purposes.



272

### 273 **3.3. Clustering**

274 Using a classifier to group the large quantity and types of aircraft data into similar features allows  
275 us to study the primary contributors to  $PO_3$  under different chemical, solar, and meteorological conditions.  
276 To accomplish this, we employ a widely-used technique known as  $k$ -means, which has been used in a variety  
277 of applications (e.g., Beddows et al., 2009; Souri et al., 2016b; Govender and Sivakumar, 2020). In this  
278 approach, centroids are distributed randomly throughout a multi-dimensional dataset, with each centroid  
279 representing a distinct class. The algorithm proceeds to assign a label to each data point by identifying its  
280 closest Euclidean distance to the centroids. Following the labeling of all data points, the algorithm updates  
281 the centroids based on the means of the newly-labeled group. This process continues iteratively until there  
282 is minimal change in the location of the centroids. It is worth noting that  $k$ -means does not guarantee an  
283 optimal solution, so we reinitialize the classification 1000 times with a new set of initial centroids. We select  
284 the result with the lowest value for the sum of the Euclidean distance among data points and centroids to  
285 ensure the outcomes are not influenced by random seeding.

286 Redundant features in the input can significantly compromise the effectiveness of the classification,  
287 so we apply principal component analysis (PCA) to the matrix of datasets ( $Z$ ) with  $n$  data points and  $p$   
288 features to reduce the dimension to a PCA-transformed matrix of  $Z$  ( $Z'$ ) with the dimension  $n \times q$ , where  
289  $q < p$ . Despite this reduction in dimension,  $Z'$  preserves a significant variance in  $Z$ , helping us to overcome  
290 the issues of dimensionality or overfitting.

291 We select 11 features simulated by the FOAM model, many of which are set to the observed values,  
292 or their precursors are observationally-constrained. These features include: SZA, HCHO/ $NO_2$ ,  
293 HCHO $\times NO_2$ , HCHO,  $NO_2$ , pressure, temperature,  $jNO_2$ ,  $jO^1D$ ,  $H_2O$ , and  $NO_2/NO_y$   
294 ( $NO_y = NO + NO_2 + PAN + HNO_3 + \text{alkyl nitrate} + N_2O_5$ ). There are indeed correlations among these features  
295 such as SZA and  $jNO_2$ , or HCHO and HCHO $\times NO_2$ ; nonetheless, we have used PCA to eliminate the  
296 possibility of these correlated factors causing overfitting issues.

### 297 **3.4. The estimation of $PO_3$**

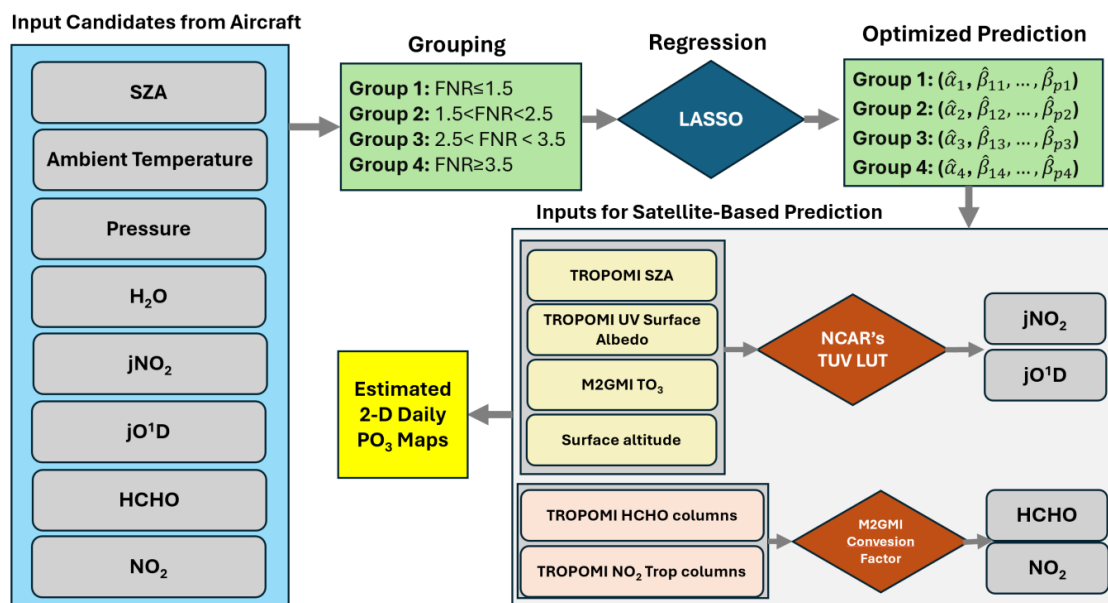
298 In order to predict  $PO_3$ , we have developed empirical equations using LASSO to link  $PO_3$  with  
299 various relevant prognostic candidates related to ozone chemistry. A schematic presenting how this  
300 estimation can be done to provide daily  $PO_3$  maps at the TROPOMI revisit time across the globe is shown  
301 in Figure 2. It is important to note that relying solely on linear regressions for a non-linear problem is not a  
302 viable approach. To address this, we have divided the data points into four distinct groups based on FNR  
303 values, meaning we divide a non-linear realm into smaller linear segments (i.e., an empirical linearization).  
304 In a study by Souri et al. (2023), a wide range of aircraft observations and box model results were used to  
305 determine that  $FNR \sim 1.7$  was a universal threshold for separating  $NO_x$ -sensitive from VOC-sensitive  
306 regimes. We have found that by breaking down the datapoints into slightly weaker or stronger variations of  
307 the regimes, we can improve the accuracy of our results. As a result, we have established four distinct  
308 groups: VOC-sensitive ( $FNR < 1.5$ ), transitions ( $1.5 < FNR < 2.5$  and  $2.5 < FNR < 3.5$ ), and  $NO_x$ -sensitive  
309 ( $FNR > 3.5$ ). The coefficients and intercepts based on the LASSO regressions for each group were computed  
310 separately. From a long list of explanatory parameters, we selected SZA, temperature, pressure,  $H_2O$ ,  $jNO_2$ ,  
311  $jO^1D$ , HCHO, and  $NO_2$  as the most sensible candidates. The reasoning behind this selection will be  
312 discussed in Section 4.2.

313 Once the LASSO parameters are determined, we applied the linear functions to variables  
314 modeled/observed in the PBL region. We show that the LASSO method votes for dropping SZA,  
315 temperature, and pressure as they do not provide significant information on  $PO_3$  compared to the rest. As  
316 for  $jNO_2$  and  $jO^1D$ , we use the TUV NCAR's LUT described in Section 2.5. HCHO and  $NO_2$  are based on  
317 converted the bias-corrected TROPOMI VCDs into PBL mixing ratios using MERRA2-GMI described in  
318 Section 2.4. To carry out the conversion, we multiply the satellite VCDs by the ratio of averaged modeled





319 mixing ratios of a target gas (i.e., NO<sub>2</sub> or HCHO) in the PBL region divided by modeled VCDs. The PBL  
 320 field also comes from MERRA2-GMI.



321

322 **Figure 2.** Schematic illustration of daily PO<sub>3</sub> estimation calculated in this study. This process consists of  
 323 two major steps: formulating PO<sub>3</sub> as a function of various prognostic inputs derived from the box model  
 324 results, and predicting PO<sub>3</sub> based on optimized features/coefficients suggested by LASSO and using  
 325 information obtained from TROPOMI, TUV, and M2GMI.

## 326 4. Results and Discussion

### 327 4.1. Box Model Validation

328 In order to assess the accuracy of the assumptions used in the box model's setup, which involves  
 329 factors such as chemical mechanism, dilution rate, and photolysis rate correction, we will compare the  
 330 simulated values of HCHO, NO<sub>2</sub>, NO, PAN, HO<sub>2</sub>, and OH with their actual measured values. This  
 331 comparison will help us determine if our model falls within an acceptable range of errors as seen in other  
 332 reputable photochemical box modeling studies. This comparison is represented in Figure 3, which displays  
 333 a scatterplot of the data collected from all seven aircraft campaigns. A discussion on each parameter follows:

334 HCHO – The box model is proficient in capturing over 77% of variance in observations with less  
 335 than 15% absolute bias. While many box modeling studies prefer to have this compound constrained to  
 336 potentially enhance the representation of HO<sub>x</sub>, it comes with the trade-off of hindering us from validating  
 337 the number/quality of observed HCHO precursors and/or the VOC treatment. Besides the study of Souri et  
 338 al. (2023), Marvin et al. (2017) is one of the few studies that did not constrain this compound to verify the  
 339 efficacy of different pathways involved in HCHO formation and loss simulated by various chemical  
 340 mechanisms. Marvin et al. (2017) reproduced HCHO formation during the SENEX campaign using the  
 341 CB06 mechanism with a R<sup>2</sup>=0.66 and a bias of 32% at 1-min averaged samples. Compared to that study,  
 342 we recreate 86% variance in observed HCHO during the same campaign with a bias of 23% (Figure S1) at  
 343 10-sec averaged samples. The remaining unresolved variance can be attributed to an incomplete list of VOC  
 344 measurements for several campaigns including DISCOVER-AQs and errors of VOCs measurements. It is



345 unlikely for the chemical mechanism to be reason for this, as Marvin et al. (2017) did not observe substantial  
346 differences in  $R^2$  values among various chemical mechanisms including the near-explicit MCM. A mild  
347 underestimation of HCHO could be likely due to the steady-state assumption, fixed arbitrary dilution factor,  
348 or uncertain isoprene chemistry (Archibald et al., 2000; Wolfe et al., 2016; Marvin et al., 2017).

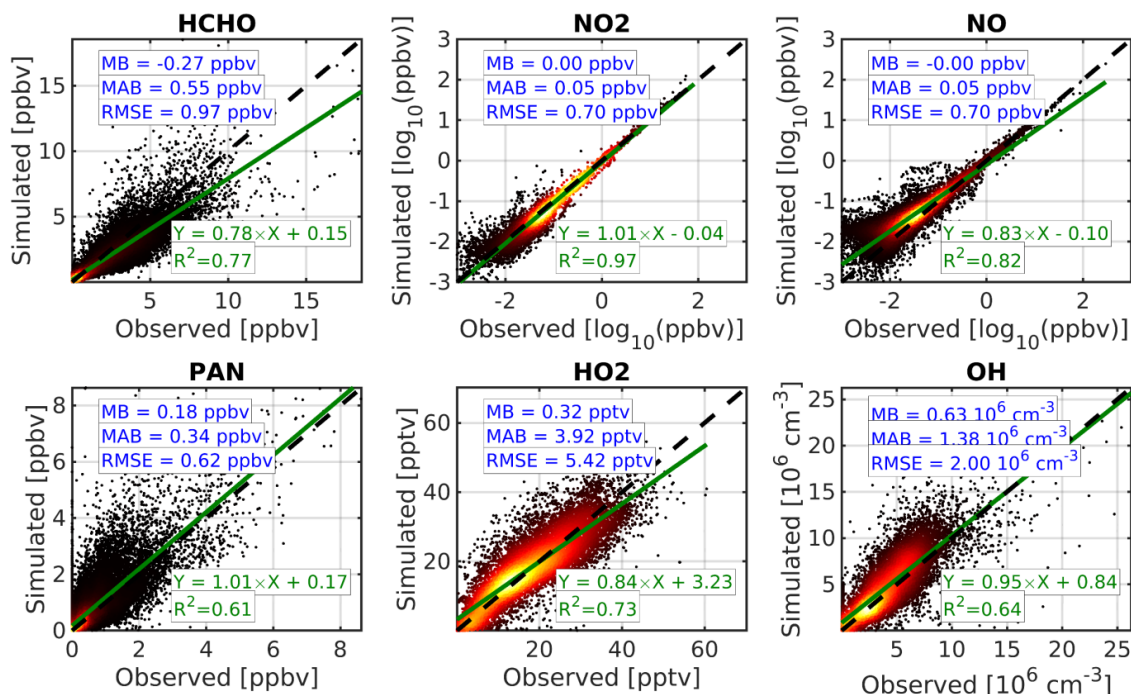
349  $\text{NO}_2$  and  $\text{NO}$  – Comparisons for both species demonstrate a high degree of correspondence for  
350 values above 0.1 ppbv. Nonetheless, we have noted a substantial amount of fluctuation in the simulations  
351 in clean regions, particularly for  $\text{NO}$ . While we cannot rule out the possibility of chemical mechanism  
352 uncertainty contributing to this deviation, the reported measurement errors for  $\text{NO}_2$  and  $\text{NO}$  are usually  
353  $\pm 0.05$  ppbv and  $\pm 0.1$  ppbv, respectively. Consequently, it is likely that the measurements error resulted in  
354 more spread in comparison.

355  $\text{PAN}$  – Our model reproduced 61% of the variance observed in  $\text{PAN}$  with a marginal absolute bias.  
356 According to Xu et al. (2021), the presence of oxygenated VOCs, particularly acetaldehyde, and the  
357  $\text{NO}/\text{NO}_2$  ratio are key factors controlling  $\text{PAN}$  levels. While we have constrained acetaldehyde, variations  
358 in the  $\text{NO}/\text{NO}_2$  ratio in heavily polluted regions (where  $\text{NO}_x$  levels exceed 1 ppbv) could potentially lead  
359 to biases in  $\text{PAN}$  simulations. Furthermore, our model's dilution factor has been arbitrarily set, and it is  
360 possible that any bias caused by this factor has been canceled out by other effects, leading to seemingly  
361 bias-free performance. However, Souri et al. (2023) showed that an incorrect dilution factor can  
362 significantly impact  $\text{PAN}$  performance, causing a sharp decline in  $R^2$  resulting in a value below 30%.  
363 Therefore, the fact that our box model has performed well with respect to  $\text{PAN}$  could be an indication that  
364 our choice of the dilution factor is not too unrealistic.

365  $\text{HO}_2$  and  $\text{OH}$  – Based on our analysis of  $\text{HO}_2$  and  $\text{OH}$  simulations during KORUS-AQ, INTEX-B,  
366 and ATOMs, we have found a reasonable level of correspondence ( $R^2 > 0.6$ ) with the performance in  
367 previous studies conducted by Souri et al. (2020), Brune et al. (2022), Miller and Brune (2022), and Souri  
368 et al. (2023) that focused on some of these campaigns. Although the box model  $\text{OH}$  simulations reported in  
369 Brune et al. (2019) during ATOMs seemed to be better than ours ( $R^2 \sim 0.8$  vs  $R^2 \sim 0.6$ ), it is important to  
370 consider that their observations were averaged over 1-minute intervals as opposed to our 30-second  
371 intervals. It should also be noted that there can be large errors in ATHOS  $\text{HO}_x$  measurements of up to  $\pm 40\%$   
372 (Miller et al., 2022), so recreating the exact variance in the observations should not be the main objective.  
373 Nonetheless, the performance of our simulations in terms of  $\text{HO}_x$  compared to observations suggests that  
374 the number of measured compounds and chemical mechanisms used in the model was effective. Our  
375 model's performance with respect to  $\text{HO}_x$  is comparable to more sophisticated mechanisms that encompass  
376 a larger number of measured species (Brune et al., 2022; Miller and Brune, 2022).

377 Overall, while there are inevitably some differences between the box model results and  
378 observations, they are consistent with what other studies have found in similar aircraft campaigns. Our  
379 extensive box model results, which consider a variety of meteorological, chemical, and photolysis rates,  
380 demonstrate satisfactory results for unconstrained compounds across a wide range of atmospheric  
381 conditions. This suggests that our training dataset from the box model is a reliable source for understanding  
382 local  $\text{PO}_3$ .

383 It is important to note that even if a simulated data point does not match up perfectly with actual  
384 observations, it still plays a role in establishing  $\text{PO}_3$  and other explanatory variables. Hypothetically, one  
385 can generate synthetic training data points by running the box model under random numbers for the inputs;  
386 but only a fraction of those can be truly observed in nature. Therefore, a mild outlier in our training dataset  
387 should be viewed as less likely to occur in nature (presuming that these campaigns could represent all  
388 conditions happening in nature), but still a valuable data point drawn from a physical model that can be  
389 used to bridge  $\text{PO}_3$  with explanatory variables.



39

391 **Figure 3.** The scatterplot comparison of simulations with observed concentrations for six unconstrained  
 392 species. More than ~133,000 observations are used for HCHO, NO<sub>2</sub>, NO, and PAN. HO<sub>x</sub> data points are  
 393 limited to ~55,000 observations. Heat maps show the density of the data. Linear fits are calculated using  
 394 the least squares method. A high R<sup>2</sup> value for HCHO indicates reasonable VOC mechanism and  
 395 measurements, given that some aircraft campaigns measured only a handful of VOCs. A relatively high R<sup>2</sup>  
 396 with minimal bias for PAN implies that the choice of the dilution factor is not unrealistic. A good  
 397 representation of HO<sub>x</sub> can indicate a reasonable prediction of the HO<sub>x</sub>-RO<sub>x</sub> cycle controlling PO<sub>3</sub>.

#### 398 4.2. Classification of aircraft data

399 Following the method described in Section 3.3, we cluster the cloud of aircraft data (~ 133k points)  
 400 into seven distinct classes. We describe them using three categories: pollution level, altitude, and SZA.  
 401 Figure 4 illustrates the violin plot of these classes for various chemical, solar, and meteorological  
 402 conditions. Figure 5 shows their corresponding violin plot of simulated PO<sub>3</sub>. A discussion of each class and  
 403 their relationship to PO<sub>3</sub> follows:

404 C1 (clean, high altitude, high SZA) – Characterized by high altitude flights, cold ambient temperature, and  
 405 negligible water vapor content, this class consists of observations that were typically taken during relatively  
 406 high SZA with a median of 50°. While high altitude observations in clear-sky conditions often should have  
 407 large photolysis rates due to reduced overhead ozone, the relatively high SZA of this class leads to low  
 408 photolysis rates. FNRs tend to be large in this class due to a higher amount of HCHO over NO<sub>2</sub>, and FNP  
 409 (HCHO×NO<sub>2</sub>) and NO<sub>2</sub>/NO<sub>y</sub> ratios are low due to the pristine conditions. The lack of sufficient ozone  
 410 precursors and reduced photochemistry make this class undergo the lowest PO<sub>3</sub> rates with a median of 0.11  
 411 ppbv/hr.

412 C2 (clean, high altitude, low SZA) - This category represents samples collected in low SZA conditions,  
 413 resulting in the highest photolysis rates among all classes. The mass of ozone precursors and the ozone



414 sensitivity condition are similar to those in C1. However, C2 PO<sub>3</sub> rates are approximately 60% higher than  
415 C1 due to increased photochemistry.

416 C3 (moderately clean, medium altitude, high SZA) - This class is characterized by observations collected  
417 in mid-altitudes and high SZA. Airsheds in C3 experienced relatively more polluted air compared to C1  
418 and C2 due to being closer to the surface. Photolysis rates are smaller than C1 possibly because of higher  
419 ozone overhead, although we cannot rule out the varying surface albedo between the classes. Despite the  
420 lower photolysis rates, C3 PO<sub>3</sub> (0.28 ppbv/hr) is larger than that of C2 and C1, indicating that pollution  
421 levels can have a more significant impact than favorable conditions for photochemistry.

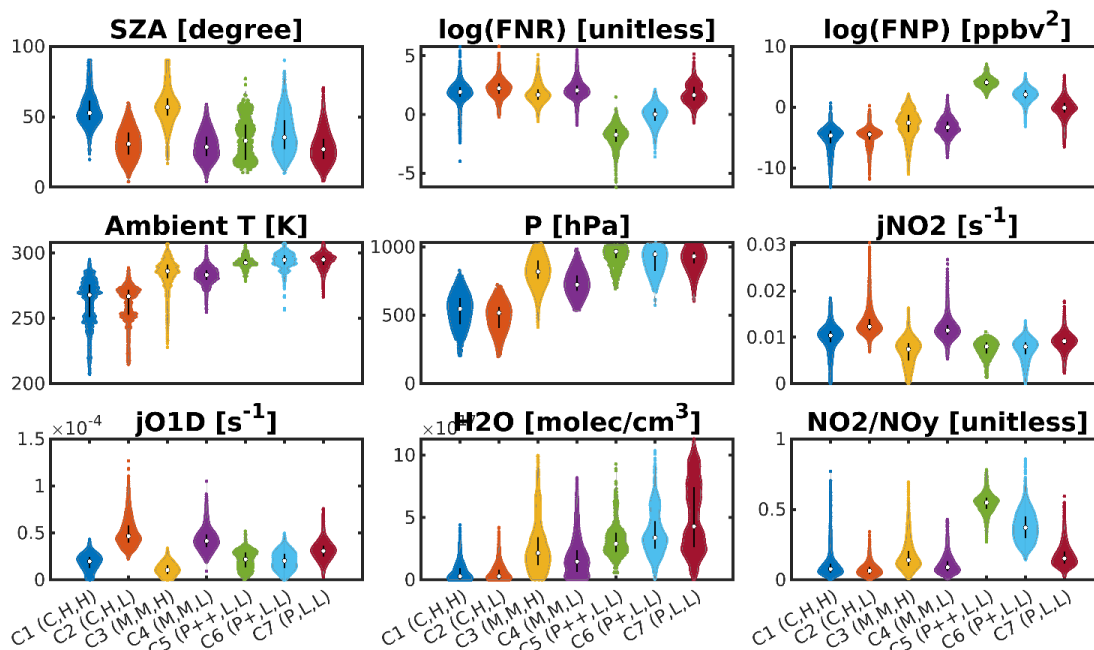
422 C4 (moderately clean, medium altitude, low SZA) - This category is distinct from C3 in terms of lower  
423 SZA (resulting in more photochemistry) and a slightly smaller number of ozone precursors. As a result of  
424 the lower ozone precursor concentration, not only is C4 PO<sub>3</sub> (0.19 ppbv/hr) lower than C3, but also is not  
425 significantly different from C2. This again implies that the amount of ozone precursors is more important  
426 than the photochemistry for these conditions.

427 C5 (extremely polluted, low altitude, low SZA) - This class features the highest amount of ozone precursors  
428 (median FNP ~ 58 ppbv<sup>2</sup>) among all classes. Furthermore, it is characterized by low photolysis rates due to  
429 its proximity to the surface, and high NO<sub>2</sub>/NO<sub>y</sub> indicative of localized polluted airshed. Unlike the previous  
430 classes, this class has the lowest FNR, indicating that it is mainly located in the VOC-sensitive regime. C5  
431 PO<sub>3</sub> values are much higher than the previous classes, with a value of 3.0 ppbv/hr.

432 C6 (polluted, low altitude, low SZA) - While this class shares similar features with C5 in terms of altitude,  
433 photolysis rates, and meteorology, it experiences a lower FNP (median of 8 ppbv<sup>2</sup>). Despite the lower FNP,  
434 C6 has the highest amount of PO<sub>3</sub> (5.2 ppbv/hr) among all classes. This is a result of reduced non-linearities,  
435 as this class does not often fall into an extreme VOC-sensitive regime (median FNR ~ 1.0) where nitrogen  
436 oxides (NO<sub>x</sub>) can hamper ozone production. This tendency coincides with Souri et al. (2023) which also  
437 found that the highest amount of PO<sub>3</sub>, lied between the transitional regimes, gravitated towards VOC-  
438 sensitive because of abundant ozone precursors and reduced negative chemical feedback of NO<sub>x</sub>.

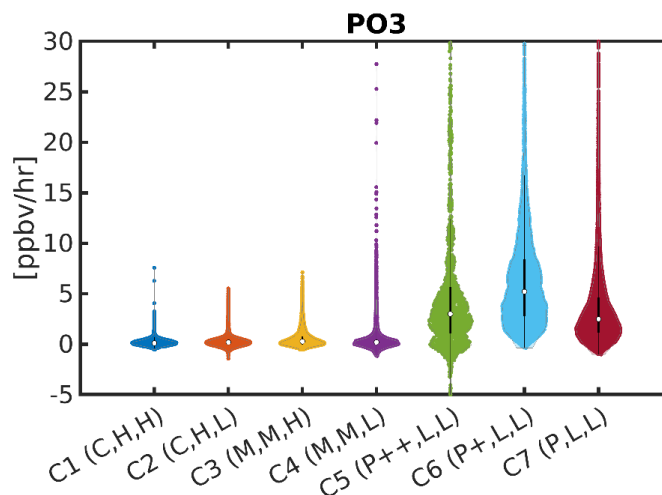
439 C7 (moderately polluted, low altitude, high SZA) - C7 is characterized by aged air close to the surface with  
440 slightly higher photolysis rates than C5 and C6. C7 PO<sub>3</sub> is 2.5 ppbv/hr, only slightly smaller than C5 despite  
441 much lower FNP (median of 0.9 ppbv<sup>2</sup>). This could be caused by the combined effect of higher photolysis  
442 rates and reduced non-linear ozone chemistry.

443 The analysis of aircraft data has revealed that the levels of HCHO and NO<sub>2</sub>, as well as the rates of  
444 jNO<sub>2</sub> and jO<sup>1</sup>D photolysis, play an important role in influencing PO<sub>3</sub>. Additionally, FNRs can offer insights  
445 into the sensitivity of PO<sub>3</sub> to its main precursors. These findings align with numerous other studies that  
446 have examined the factors driving PO<sub>3</sub> (e.g., Duncan and Chameides, 1998; Thornton et al., 2002; Kleiman  
447 et al., 2002; Gerasopoulos et al., 2006; Chatfield et al., 2010; Baylon et al., 2018; Wang et al., 2020; Souri  
448 et al., 2023). Consequently, our PO<sub>3</sub> estimates will incorporate HCHO, NO<sub>2</sub>, jNO<sub>2</sub>, jO<sup>1</sup>D, and FNR. While  
449 the cluster analysis did not definitively indicate whether meteorological conditions impact PO<sub>3</sub>, we will  
450 also include ambient temperature, water vapor, pressure, and SZA to determine if they provide any  
451 additional insights into PO<sub>3</sub> estimates.



452

453 **Figure 4.** The violin plots of six different parameters coming from the box model clustered into seven  
 454 distinct categories. Each cluster is described by three labels: air pollution levels (C: clean, M: moderately  
 455 clean, P: moderately polluted, P+: polluted, P++: extremely polluted), altitude (H: high, M: medium, L:  
 456 low), and SZA (H: high, L: low). The white dot is the median and the bars explain the 75<sup>th</sup> and 25<sup>th</sup>  
 457 percentiles.



458

459 **Figure 5.** The corresponding violin plots of simulated PO<sub>3</sub> for the seven clusters described in Figure 4.  
 460 The lowest PO<sub>3</sub> is seen in remote regions (C-M) where ozone precursors are minimal. The highest PO<sub>3</sub>  
 461 does not happen in the most polluted region (P++) resulting from the non-linear ozone chemistry.





462 **4.3. Estimates of PO<sub>3</sub>**

463 **4.3.1. LASSO coefficients**

464 Armed with a procedure that finds the important features in a linear model (Section 3.1), we now  
 465 explore utilizing LASSO for PO<sub>3</sub> estimation. We are leveraging all data points generated by the  
 466 observationally-constrained box model from various atmospheric composition campaigns. Among the  
 467 selected variables shown in Figure 2, the LASSO algorithm assigns zero coefficients to SZA, pressure,  
 468 temperature, and water vapor, indicating that they offer less valuable information compared to other  
 469 variables. This decision was made by systematically adjusting the regularization factor within a 10-fold  
 470 cross-validation framework to identify the optimal factor that strikes a balance between solution variance  
 471 and prediction bias. As a result, the LASSO algorithm suggests that HCHO, NO<sub>2</sub>, jNO<sub>2</sub>, and jO<sup>1</sup>D contain  
 472 sufficient information to accurately predict PO<sub>3</sub> for the most part.

473 Table 1 provides the intercepts and the corresponding coefficients for four different regions  
 474 separated by FNR. While we do not expect for a statistical model to fully single out the “cause and effect”  
 475 relationship between explanatory variables and the target, we note that it has some basic understanding of  
 476 ozone chemistry; the HCHO coefficients increase as moving towards smaller FNRs (i.e., more VOC-  
 477 sensitive). The same tendency is evident with respect to NO<sub>2</sub> and larger FNRs (i.e., more NO<sub>x</sub>-sensitive).  
 478 The negative coefficient of NO<sub>2</sub> in regions having FNR≤1.5, implies some levels of non-linear feedback  
 479 embedded in this parameterization. Both jNO<sub>2</sub> and JO<sup>1</sup>D have positive coefficients throughout the chemical  
 480 conditions, suggesting that more photolysis rates accelerate PO<sub>3</sub>. JO<sup>1</sup>D has a smaller effect than jNO<sub>2</sub> on  
 481 PO<sub>3</sub> over remote regions (FNR≥3.5) perhaps because of redundant information available compared to jNO<sub>2</sub>.

482 **Table 1.** Calibrated coefficients derived from the LASSO estimator using seven atmospheric  
 483 composition aircraft campaigns.

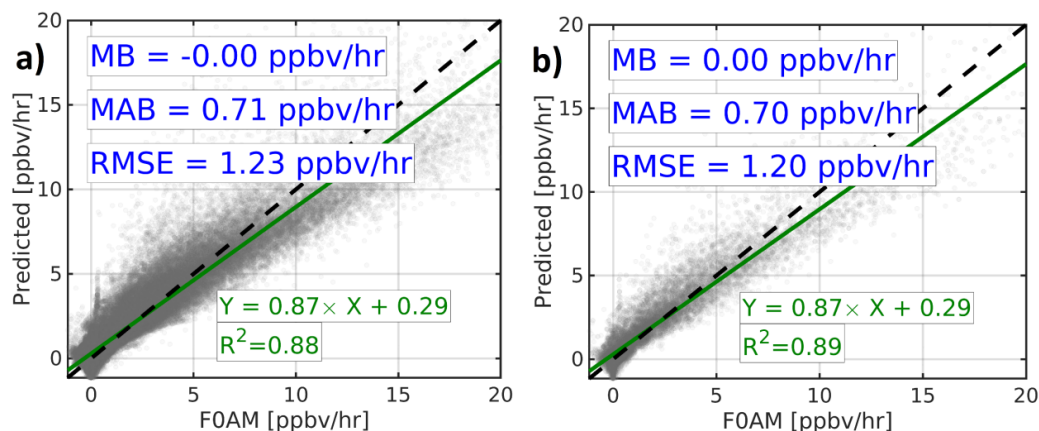
Group	Criteria for FNR	Intercept	HCHO [ppbv]	NO <sub>2</sub> [ppbv]	jNO <sub>2</sub> ×10 <sup>3</sup> [s <sup>-1</sup> ]	jO <sup>1</sup> D×10 <sup>6</sup> [s <sup>-1</sup> ]
1	FNR≤1.5	-1.98	1.85	-0.14	0.12	0.09
2	1.5<FNR<2.5	-3.38	1.79	0.98	0.19	0.07
3	2.5<FNR<3.5	-3.27	1.07	3.48	0.21	0.03
4	FNR≥3.5	-1.63	0.41	6.54	0.11	0.01

484

485 **4.3.2. Validation of PO<sub>3</sub> predictions**

486 The validation of PO<sub>3</sub> prediction against the box model results is performed in threefold with an  
 487 increasing stringency order: i) using all data points used in the LASSO algorithm, ii) by random dropping  
 488 data points, and iii) by dropping each air quality campaign from the LASSO estimation and using its data  
 489 as benchmark.

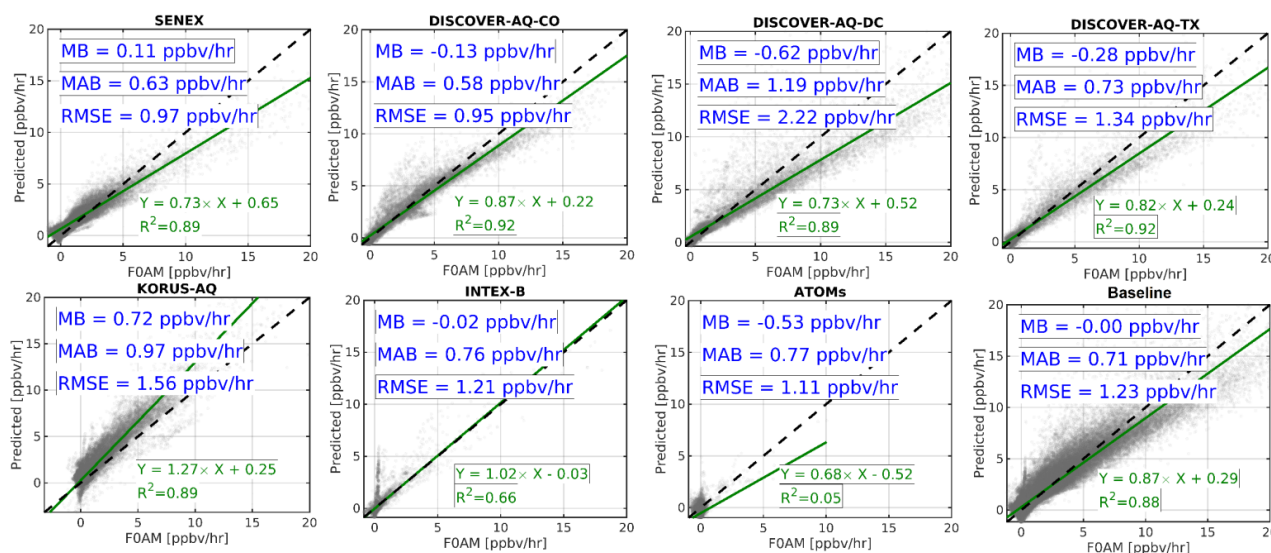
490 Figure 6a shows the scatterplot of predicted PO<sub>3</sub> against the box model for all data points used to  
 491 estimate the coefficients described in Section 4.3.1. Despite the algorithm's simplicity, we can recreate more  
 492 than 88% of the variance in PO<sub>3</sub> with negligible absolute bias. This has an important indication that our  
 493 scientific problem is not overly complex. There is less than 30% bias with respect to the mean absolute bias  
 494 of the prediction. The positive offset and a slope smaller than one indicate a mild underestimation  
 495 (overestimation) of PO<sub>3</sub> in polluted (clean) regions. Figure 6b shows the same analysis for 20,000 randomly  
 496 chosen data points (~15% of the total) that we purposefully dropped from the LASSO estimation to gauge  
 497 if the predictor model can replicate numbers for points not used during the training. We find almost identical  
 498 statistics for these points, suggesting that the prediction stays robust for points outside the training data set.  
 499 However, the most stringent method is to drop each campaign data set entirely to understand where the  
 500 prediction model struggles most.



501

502 **Figure 6.** Scatterplots comparing observationally-constrained FOAM model PO<sub>3</sub> and the predictions based  
 503 on the proposed algorithm for (a) all data points and (b) 20,000 randomly-dropped data points as  
 504 benchmarks. Despite the simplicity of the algorithm, we can reproduce a large variance in PO<sub>3</sub> using only  
 505 four explanatory variables.

506 Figure 7 shows several subplots pertaining to dropped campaigns from the analysis. Immediately  
 507 evident is that our PO<sub>3</sub> estimation has considerable skills at capturing PO<sub>3</sub> for most polluted cases, including  
 508 DISCOVER-AQs, KORUS-AQ, and SENEX without using their individual datasets. This provides  
 509 convincing evidence about a high degree of generalizability of the predictor. However, the model has a  
 510 reduction in performance in INTEX-B for PO<sub>3</sub> <1 ppbv/h. Moreover, the model prediction power is  
 511 consistently poor for ATOMs where a significant fraction of airsheds were samples in pristine areas. We see  
 512 such poor performance for PO<sub>3</sub><1 ppbv/hr for other campaigns such as KORUS-AQ. Therefore, it is  
 513 difficult to have confidence in the predictor power of the model in remote regions, which may be caused  
 514 by the lack of inclusion of HO<sub>x</sub>, halogens, and H<sub>2</sub>O in the fit, as they can become an important sink for  
 515 tropospheric ozone in those areas (Simpson et al., 2015). Nonetheless, while our predictive accuracy  
 516 remains poor for this specific subset of the data, the practical utility and significance of this specific region  
 517 (i.e., pristine areas) for air quality applications are notably limited. Given these results, we limit our  
 518 predictions to PO<sub>3</sub>>1 ppbv/hr for the subsequent analyses.



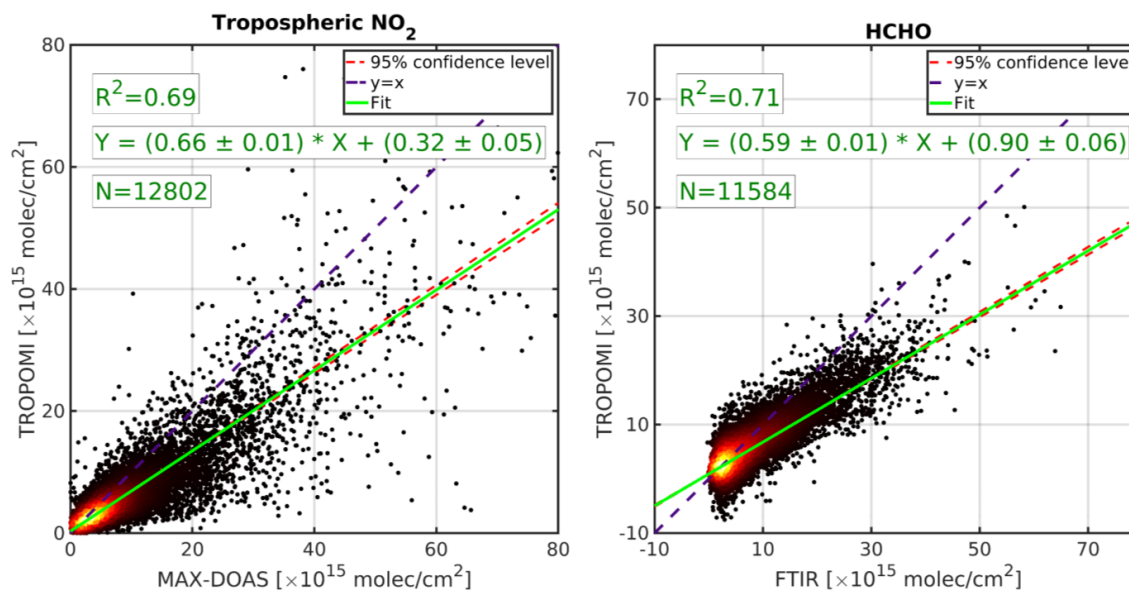
520 **Figure 7.** Same as Figure 6b, but each campaign is dropped from the LASSO estimation and subsequently  
 521 used as an independent benchmark. The designed algorithm has shown a high degree of skill at predicting  
 522  $\text{PO}_3$  in polluted regions; however, it performs poorly in pristine areas.

#### 523 4.3.3. TROPOMI $\text{NO}_2$ and HCHO validation

524 To build confidence in our quantitative application of TROPOMI data for  $\text{PO}_3$  estimates, we  
 525 validate the daily tropospheric  $\text{NO}_2$  and total HCHO columns against MAX-DOAS and FTIR observations  
 526 based upon the validation framework outlined in Vigouroux et al. (2020) and Verheolst et al. (2021). Both  
 527 paired datasets have been expanded to late 2023 showing a fuller picture of TROPOMI error  
 528 characterization compared to former studies. Figure 8 shows the comparison of daily TROPOMI, the  
 529 benchmarks and the optimal fit associated with their errors for the period of 2018-2023.

530 In the context of tropospheric  $\text{NO}_2$  comparison, we observe a slope smaller than one ( $\sim 0.66$ ) with  
 531 a positive offset ( $0.32 \times 10^{15} \text{ molec/cm}^2$ ). This tendency has been repeatedly documented in various studies  
 532 for various satellites or benchmarks (e.g., Griffin et al., 2019; Choi et al., 2020; Verheolst et al. 2021; van  
 533 Geffen et al., 2022). A slope smaller than one, originating from unresolved systematic biases, implies that  
 534 TROPOMI is biased-low in polluted regions. A slight positive offset suggests that TROPOMI  $\text{NO}_2$  is  
 535 biased-high in remote regions. The errors of slope and the offset are relatively small, evidence of the  
 536 robustness of the optimal fit against the dataset variance. Nonetheless, we will incorporate them into Eqs 2  
 537 and 3 to take the adjustment error into consideration.

538 Despite the inherent difficulty in obtaining HCHO observations from the UV-Vis imagery  
 539 (González Abad et al., 2019), the HCHO comparison exhibits a good alignment with benchmarks. Like the  
 540 previous comparison, the slope is smaller than one ( $\sim 0.59$ ) and the offset is positive ( $\sim 0.9 \times 10^{15} \text{ molec/cm}^2$ )  
 541 agreeing within 10% with studies done by Vigouroux et al. (2020) and De Smedt et al. (2021).  
 542 Consequently, we will consider the fit errors and adjust all VCDs based on the slope and the offset obtained  
 543 from this comparison.



544

545 **Figure 8.** The comparison of TROPOMI tropospheric NO<sub>2</sub> and MAX-DOAS (left) and TROPOMI HCHO  
 546 and FTIR (right). The data points cover the period of 2018-2023. Both errors of in-situ measurements and  
 547 TROPOMI are considered in the fit. The data curation procedure has been discussed in Verhoelst et al.  
 548 (2021) and Vigouroux et al. (2020). The slope smaller than one suggests that both HCHO and NO<sub>2</sub> retrievals  
 549 are underestimated in polluted regions.

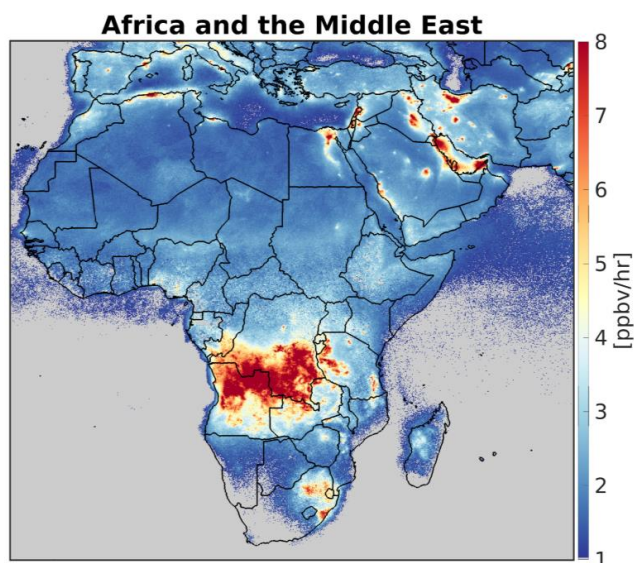
550 *4.3.4. Maps of PO<sub>3</sub> across various regions and qualitative description*

551 Taking advantage of the wealth of bias-corrected TROPOMI observations, we present the first-ever  
 552 reported PO<sub>3</sub> maps at 0.1×0.1 degrees in the PBL in July 2019 across various geographic regions. Moreover,  
 553 because of the explicit nature of our algorithm, it is straightforward to break down the contributors of PO<sub>3</sub>  
 554 to gather insights into how each driver has shaped the distribution of PO<sub>3</sub>. Therefore, in addition to PO<sub>3</sub>  
 555 maps, we will show the magnitudes of various drivers of PO<sub>3</sub> including NO<sub>2</sub>, HCHO, and FNR  
 556 concentrations in the PBL region, the sum of scaled jO<sup>1</sup>D and jNO<sub>2</sub> values, along with their contributions  
 557 to PO<sub>3</sub>. It is worth noting that these maps are only a snapshot of PO<sub>3</sub> whose precursors can have large  
 558 interannual and interdecadal variability caused by meteorology, chemistry, and emissions. A discussion on  
 559 each region follows:

560 *Africa and the Middle East* – Figure 9 illustrates the significant rates of PO<sub>3</sub> over the region, particularly  
 561 concentrated over major cities such as Tehran (Iran), Cairo (Egypt), Riyadh (Saudi), Baghdad (Iraq), Algiers  
 562 (Algeria), and Johannesburg (South Africa). These urban areas consistently experience poor air quality  
 563 episodes (e.g., Chaichan et al., 2016; Belhout et al., 2018; Yousefian et al., 2020; Thompson et al., 2014;  
 564 Boraiy et al., 2023; Choi and Sourì et al. 2015a). The biomass burning activities in Africa (see Figure 1 in  
 565 Roberts et al., 2009) significantly contribute to the high rates of PO<sub>3</sub>. Moreover, we see accelerated PO<sub>3</sub>  
 566 over the Persian Gulf, a region housing oil and gas production facilities, leading to high PO<sub>3</sub> in the region  
 567 (Lelieveld et al., 2009; Choi and Sourì et al. 2015a). Figure 10 shows NO<sub>2</sub> and HCHO concentrations are  
 568 highly correlated in the Middle East ( $r=0.82$ ) due to co-emitted NO<sub>x</sub> and VOC emissions, predominantly  
 569 from anthropogenic sources. Over the whole region, HCHO and NO<sub>2</sub> concentrations are only moderately  
 570 correlated ( $r=0.61$ ). This is because there is strong spatial heterogeneity associated with NO<sub>x</sub> and VOC  
 571 emissions over Africa that are not spatially correlated. One possible explanation for this could be the  
 572 emission dependence on the type of fire combustion in Africa (van der Velde et al., 2021) and the location



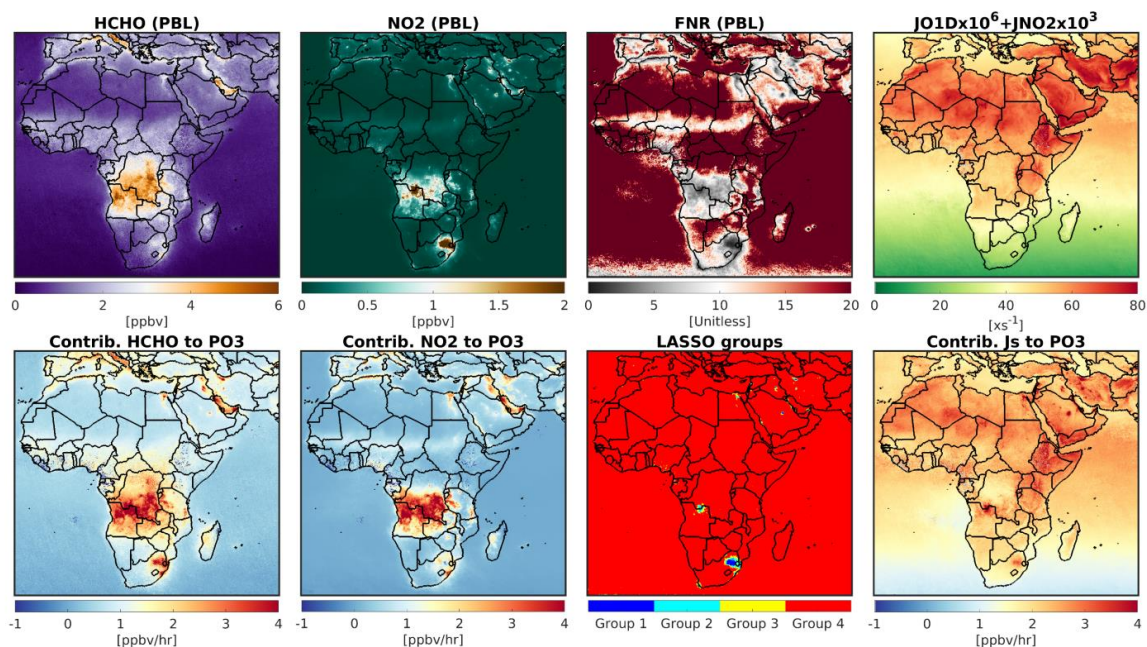
573 of biogenic isoprene emissions (Marais et al., 2014). For the most part, FNRs tend to fall in ranges above  
574  $>3.5$  (LASSO group 4, highly  $\text{NO}_x$ -sensitive). However, lower FNRs are prevalent in the core of cities due  
575 to elevated  $\text{NO}_x$  emissions. The contributions of HCHO to  $\text{PO}_3$  occur predominantly over areas with low  
576 FNRs. These results suggest that  $\text{NO}_x$  emissions dictate the location of maximum VOC contributions to  
577  $\text{PO}_3$ . The contribution of  $\text{NO}_2$  to  $\text{PO}_3$  behaves non-linearly with negative values at the core of cities such as  
578 Johannesburg and Tehran (Figure S2). Photolysis rates are high over low SZA and bright surface albedo  
579 (i.e., arid land). Accordingly, photolysis rates exhibit a latitudinal gradient in response to changes in SZA.  
580 Greater contributions of photolysis rates to  $\text{PO}_3$  are observed in areas with low FNRs, as determined by the  
581 LASSO estimator (Table 1).



582

583 **Figure 9.** The spatial distribution of  $\text{PO}_3$  within the PBL region averaged over July 2019 in Africa and the  
584 Middle East.  $\text{PO}_3 < 1$  ppbv/hr is masked due to the algorithm deficiencies. Accelerated  $\text{PO}_3$  can be seen over  
585 major cities and biomass burning activities in Africa.

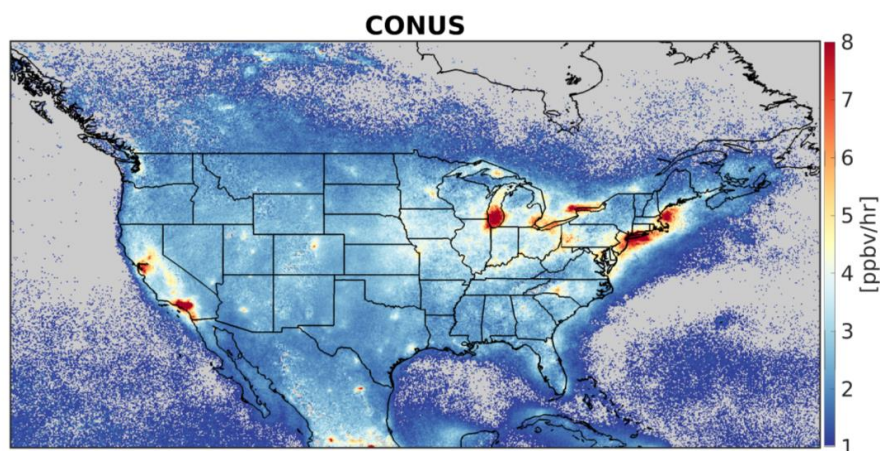




586

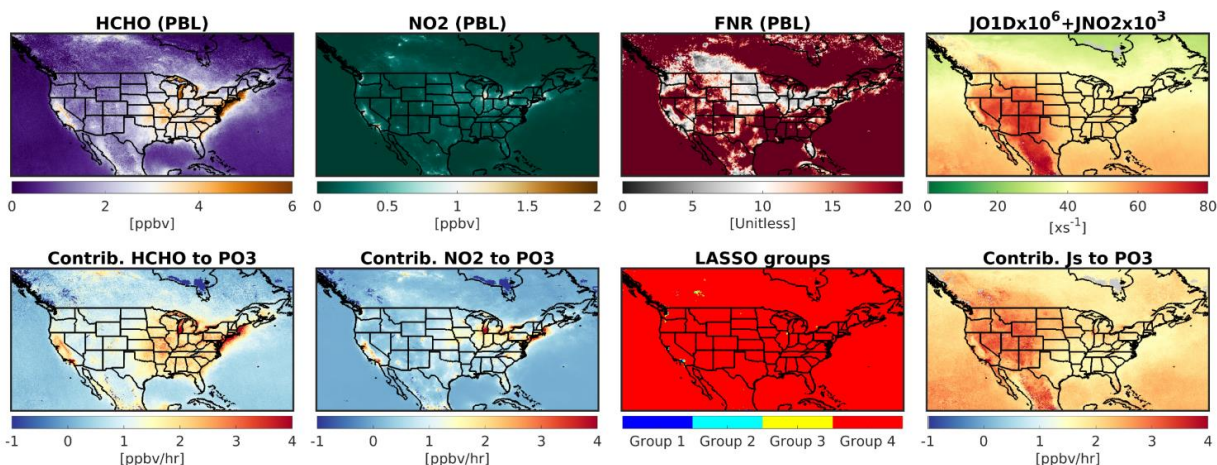
587 **Figure 10.** (first row) PBL concentrations of HCHO, NO<sub>2</sub>, FNR and sum of scaled jO<sup>1</sup>D and jNO<sub>2</sub> derived  
 588 from TROPOMI and models in July 2019; (second row) the contributions of HCHO, NO<sub>2</sub>, and photolysis  
 589 rates to PO<sub>3</sub>, along with the defined LASSO ozone production sensitivity regimes for PO<sub>3</sub> estimates.

590 *Contiguous United States* – New York City, Los Angeles (LA), the San Francisco Bay area, and Lake  
 591 Michigan areas all experience accelerated PO<sub>3</sub> in July 2019, as shown in Figure 11. All the regions fall into  
 592 non-attainment regions (marginal to extreme) with respect to ozone standards and have been immensely  
 593 studied (Wu et al., 2024; Kim et al., 2022; Stainer et al., 2021). While it requires several physical processes,  
 594 such as vertical and horizontal transport, to translate these PO<sub>3</sub> rates into ozone concentrations, applying  
 595 this product in locating the hotspot of ozone polluters shows promise. Except for LA, the vast majority of  
 596 CONUS fall into large FNRs (>3.5), making NO<sub>2</sub> levels largely shape the spatial distribution of PO<sub>3</sub> (Figure  
 597 12). HCHO levels are found to be relatively large over LA, causing PO<sub>3</sub> to increase due to its greater  
 598 sensitivity to VOCs. In addition to high levels of HCHO and NO<sub>2</sub> in several Californian regions, accelerated  
 599 photochemistry caused by the bright surface albedo enhances PO<sub>3</sub>.



600

601 **Figure 11.** Same as Figure 9 but for CONUS. Elevated PO<sub>3</sub> prevails over various areas such as New York  
602 City, Los Angeles, San Francisco Bay area, and Lake Michigan.

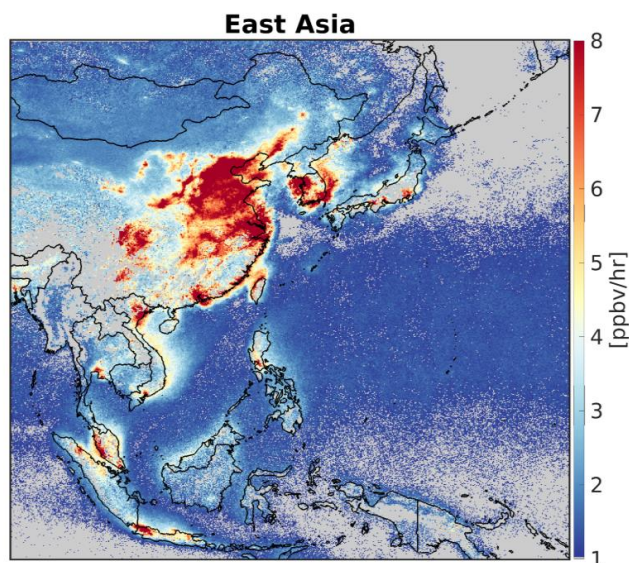


€

604 **Figure 12.** Same as Figure 10 but for CONUS.

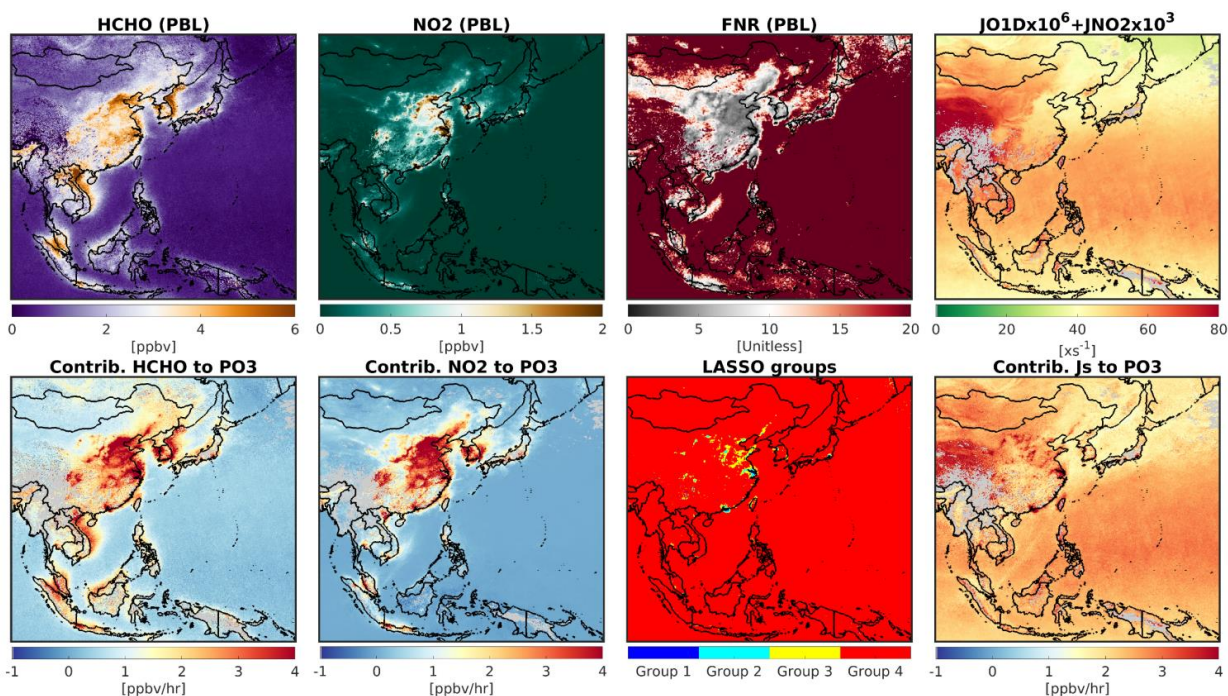
605 *East and Southeast Asia* – Figure 13 shows extremely accelerated PO<sub>3</sub> values over East Asia, particularly  
606 over North China Plain, Yangtze River Delta, Pearl River Delta, and Seoul. These regions have experienced  
607 severely degraded air quality with respect to ozone (Souri et al., 2020a,b; Li et al., 2019; Colombi et al.,  
608 2023; Schroeder et al., 2020; Wang et al., 2017; Zhang et al., 2007). In southeast Asia, Hanoi (Vietnam),  
609 Kuala Lumpur (Malaysia), and Jakarta (Indonesia), undergoing heightened PO<sub>3</sub> as well, have received less  
610 attention in literature (Ahamad et al., 2020; Kusumaningtyas et al., 2024; Sakamoto et al., 2018). Figure 14  
611 suggests that the chemical condition of many regions in China and South Korea, falling within the  
612 transitional regimes (LASSO group 2 and 3, 1.5 < FNR < 3.5), has made them susceptible to high PO<sub>3</sub> levels  
613 due to concurrent high concentrations of HCHO and NO<sub>2</sub>. Moreover, photochemistry appears to be active  
614 throughout the region.





615

616 **Figure 13.** Same as Figure 9 but for east and southeast Asia. Because of heightened amount of  
 617 photochemistry, NO<sub>2</sub>, and HCHO, we observe accelerated PO<sub>3</sub> throughout the majority of the cities in East  
 618 and Southeast Asia.

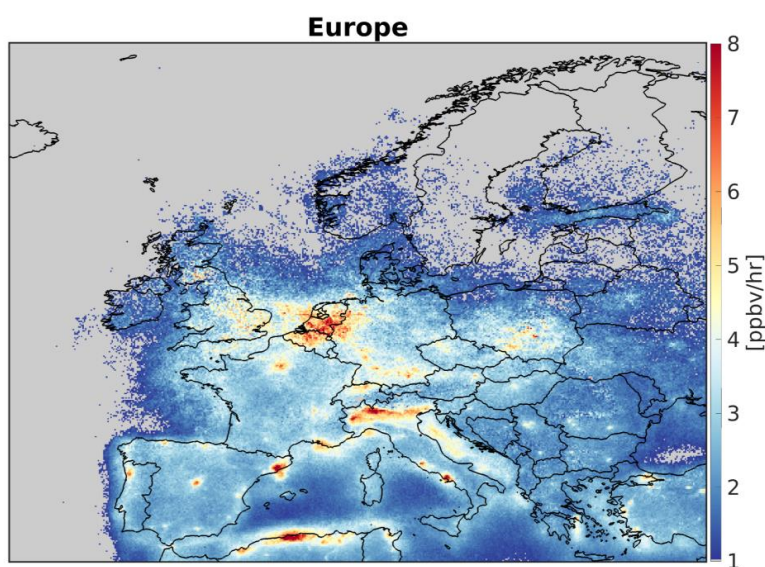


6



620 **Figure 14.** Same as Figure 10 but for east and southeast Asia.

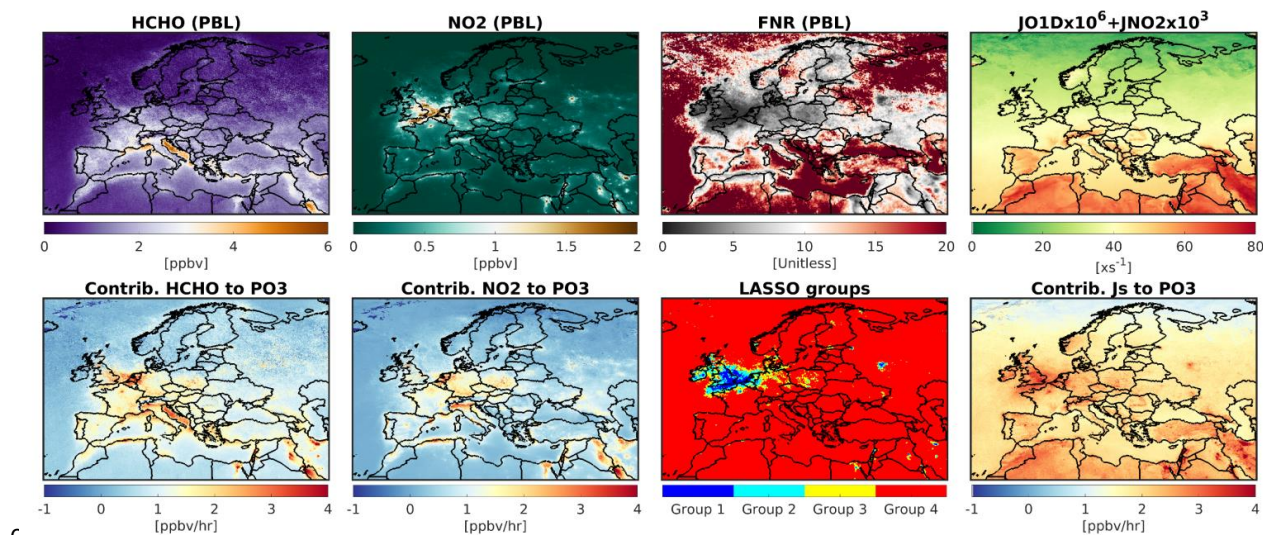
621 *Europe* – Figure 15 reveals high  $\text{PO}_3$  over Benelux, Po Valley (Italy), and several major cities such as  
622 Barcelona (Spain) and Rome (Italy). Benelux has the largest hotspot of  $\text{PO}_3$  in the region (e.g., Zara et al.,  
623 2021). A significant portion of England, Benelux, fall into VOC-sensitive, or the transitional regime  
624 ( $\text{FNR} < 2.5$ ) shown in Figure 16. Because of diminished photochemistry in these high latitude regions, we  
625 do not see significant PBL concentrations of HCHO in order for  $\text{PO}_3$  to be as high as the previous areas;  
626 moreover, the non-linear  $\text{NO}_x$  feedback has led to negative contributions of  $\text{NO}_2$  to  $\text{PO}_3$  in several cities  
627 such as London. In general, low photolysis rates compared to the previous regions have made most of  
628 Europe less prone to elevated  $\text{PO}_3$ .



629

630 **Figure 15.** Same as Figure 9 but for Europe. Because of reduced photochemistry,  $\text{PO}_3$  values tend to be  
631 smaller than the previous cases. Benelux has experienced the highest  $\text{PO}_3$  in this region.





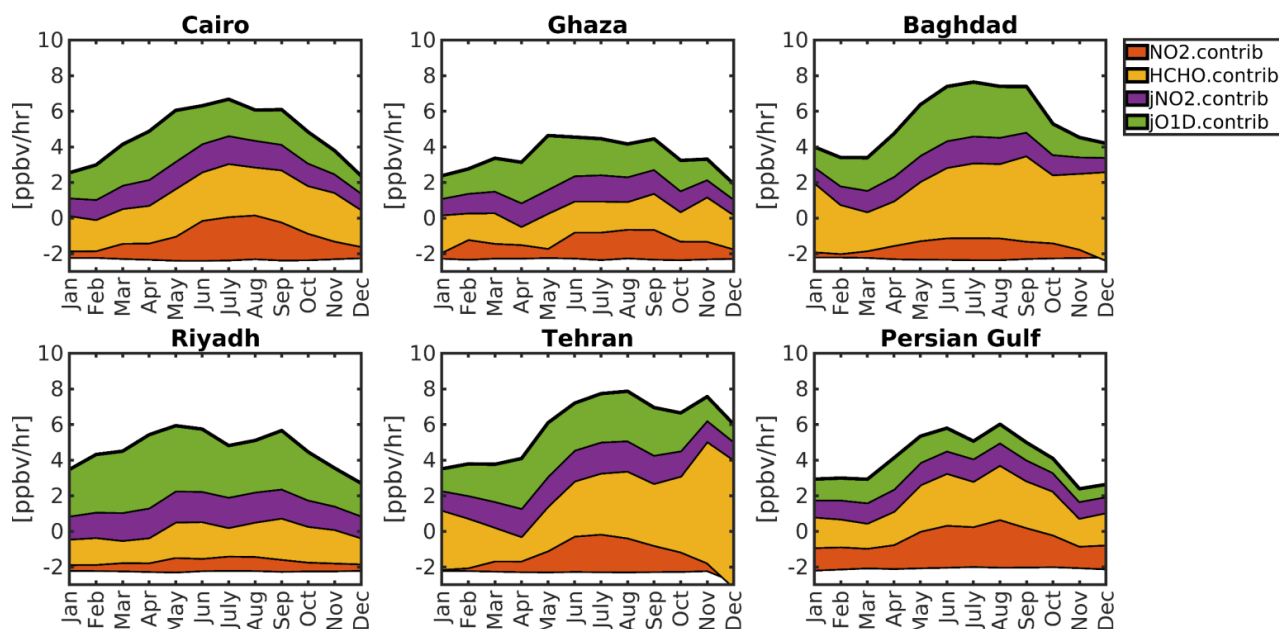
€ **Figure 16.** Same as Figure 10 but for Europe.

#### 634 4.3.5. Seasonality of $PO_3$ over the Middle East

635 It is attractive to study the seasonal variations in the contributors to  $PO_3$  over several major cities  
 636 because the  $PO_3$  drivers' seasonality can vary from location to location. We decide to focus on several  
 637 Middle Eastern countries that have experienced rapid growth and degraded air quality: Cairo (Egypt),  
 638 Ghaza (Palestine), Baghdad (Iraq), Riyadh (Saudi Arabia), Tehran (Iran), and the Persian Gulf region. We  
 639 illustrate the seasonality of four major contributors to  $PO_3$  including  $NO_2$ , HCHO,  $jNO_2$ , and  $jO^1D$  in 2019  
 640 in Figure 17.

641 The levels of HCHO (a proxy for VOCs) consistently have the greatest impact on  $PO_3$  throughout  
 642 the year in these regions. Specifically, both Baghdad and Tehran experience high levels of HCHO even  
 643 during colder months, which can be observed using TROPOMI. This suggests that regulations targeting the  
 644 reduction of man-made VOC emissions should be prioritized in this region.  $PO_3$  levels over Cairo, Gaza,  
 645 Baghdad, and the Persian Gulf peak during summertime, while Tehran experiences a comparable peak in  
 646 the autumn due to increased VOC emissions. Additionally, we notice a decrease in  $PO_3$  levels over the  
 647 Persian Gulf and Riyadh in July, possibly due to a decline in HCHO contributions caused by meteorological  
 648 factors. Even though  $NO_2$  concentrations decline in summertime due to shorter lifetime against OH, the  
 649 higher amount of HCHO makes  $PO_3$  more sensitive to  $NO_2$  in this season. Ghaza shows the least seasonal  
 650 variation among these regions, likely due to consistently active photochemistry throughout the year.



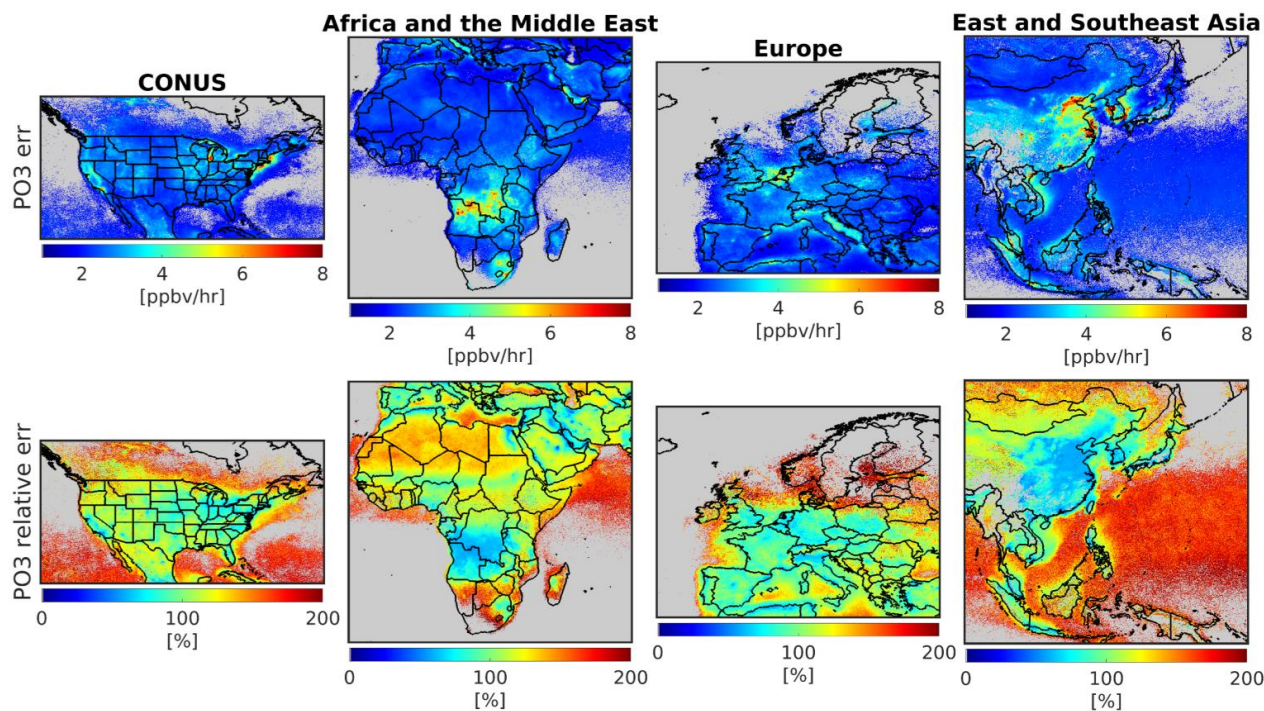


652 **Figure 17.** The contributions of NO<sub>2</sub>, HCHO, jNO<sub>2</sub>, and jO<sup>1</sup>D to the PBL PO<sub>3</sub> for several major regions in  
 653 the Middle East. The data is based on 2019 TROPOMI observations. PO<sub>3</sub> tends to spike around the summer  
 654 due to increased HCHO, higher sensitivity of PO<sub>3</sub> to NO<sub>x</sub>, and enhanced photochemistry. However, Tehran  
 655 shows a second peak in autumn due to unusual high values of HCHO.

#### 656 4.3.6. The effect of satellite errors on PO<sub>3</sub>

657 Satellite retrieval errors have been identified as the primary obstacle to achieving a robust  
 658 understanding of ozone chemistry using HCHO and NO<sub>2</sub> data (Souri et al., 2023; Johnson et al., 2023);  
 659 therefore, generating uncertainty maps is crucial for informing the scientific community about the  
 660 credibility of our PO<sub>3</sub> estimates. In this study, we utilize the equations outlined in Section 2.2.1 to propagate  
 661 the errors of HCHO and NO<sub>2</sub> retrievals to the final PO<sub>3</sub> estimates. We achieve this by recalculating the PO<sub>3</sub>  
 662 value for a given pixel 10,000 times, with each recalculation based on a sample drawn from a normal  
 663 distribution with a standard deviation equal to the satellite total error. The standard deviation of these  
 664 samples offers a good approximation of the impact of satellite errors on PO<sub>3</sub> estimates.

665 Figure 18 illustrates the maps of PO<sub>3</sub> absolute and relative errors over the targeted regions in the  
 666 course of the month of July. The errors of PO<sub>3</sub> estimates tend to be markedly high (100-300%) in remote  
 667 regions where the trace gas signals are small. However, the PO<sub>3</sub> errors are within 40-60% in polluted regions  
 668 where the signals are larger. Currently, the absence of absolute measurements of PO<sub>3</sub> at this vast spatial  
 669 coverage makes it challenging to judge the severity of these errors for PO<sub>3</sub> applications. Nonetheless, any  
 670 application based on this product should be recalculated within the reported errors through a Monte-Carlo  
 671 to gauge the significance of the outcome.



---

673 **Figure 18.** The influence of the satellite errors on  $PO_3$  estimates (absolute and relative) over four major  
 674 regions tackled in this work. The errors are based on monthly-averaged TROPOMI errors. The errors tend  
 675 to be mild over polluted regions (40-60%) but they can exceed above 100% over pristine ones.

## 676 5. Conclusion

677 Providing data-driven and integrated maps of ozone production rates ( $PO_3$ ) using remote sensing  
 678 sensors enabled us to generate the first satellite-derived product of this kind, offering extensive spatial  
 679 coverage with significant applications in atmospheric chemistry. This data has indeed extended the use of  
 680 formaldehyde (HCHO) over nitrogen dioxide ( $NO_2$ ) ratios (FNR) beyond their current role. Through this  
 681 product, we can shed light on the effects of emission regulations, wildfires, widespread lockdown, wars,  
 682 and economic recessions on  $PO_3$  levels. Furthermore, given the long-term records of satellite observations  
 683 (e.g., OMI since 2005 and TROPOMI since 2018), this product can inform emission regulators about  
 684 locally-produced ozone hotspots, and ultimately, enhance our understanding of the spatiotemporal  
 685 variability of ozone formation for over two decades.

686 In this study, we generated maps of within the planetary boundary layer (PBL), constrained by bias-  
 687 corrected TROPospheric Monitoring Instrument (TROPOMI) observations, using a piecewise regularized  
 688 regression model. This model was calibrated using a blend of data from a comprehensive suite of aircraft  
 689 observations and a well-characterized box model. These maps, produced for various regions, allowed us to  
 690 identify hotspots of locally-produced ozone pollution with unprecedented resolution. Our findings indicated  
 691 that numerous urban areas in the Middle East, East Asia, and Southeast Asia exhibit accelerated  $PO_3$  rates  
 692 ( $>10$  ppbv/hr), attributed to high levels of anthropogenic nitrogen oxides ( $NO_x = NO + NO_2$ ), volatile  
 693 organic compounds (VOCs), and active photochemistry. In contrast, such elevated  $PO_3$  levels were less  
 694 prevalent in the United States and Europe, with exceptions including Los Angeles, New York City, and the



695 entire region of the Benelux. Additionally, biomass burning activities in Africa contributed to significant  
696  $\text{PO}_3$  levels across extensive areas. Seasonality of  $\text{PO}_3$  peaked around the summer for several regions in the  
697 Middle East because of active photochemistry and concurrent large HCHO and  $\text{NO}_2$  levels; however,  
698 Tehran experienced elevated  $\text{PO}_3$  in the autumn due to large HCHO values possibly produced from  
699 anthropogenic emissions.

700 The production of these maps relied heavily on a robust training dataset. To this end, we  
701 incorporated an extensive array of aircraft observations from multiple atmospheric composition campaigns,  
702 including DISCOVER-AQ, KORUS-AQ, INTEX-B, ATOM, and SENEX, into the Framework for 0-D  
703 Atmospheric Modeling (F0AM) photochemical box model. The box model demonstrated a high level of  
704 correspondence ( $R^2 > 0.6$ , with minimal biases) between several unconstrained compounds (e.g., HCHO,  
705 OH,  $\text{HO}_2$ , PAN, NO, and  $\text{NO}_2$ ) and their observed counterparts, indicating its effectiveness in understanding  
706 local ozone chemistry. Utilizing a classification algorithm applied to the data obtained from the constrained  
707 box model, we identified HCHO,  $\text{NO}_2$ , their ratio (known as FNR), photolysis rates, and, to some extent,  
708 meteorological factors as good candidates for reproducing  $\text{PO}_3$  variability and magnitudes.

709 Subsequently, we employed a piecewise linear model known as LASSO, which is capable of  
710 feature selection by eliminating unimportant inputs, to parameterize  $\text{PO}_3$ . A key component of this  
711 parameterization was the use of FNR to empirically linearize the non-linear ozone chemistry. The LASSO  
712 algorithm indicated that more than 88% of the variance in  $\text{PO}_3$  could be reproduced with low bias using  
713 only five parameters: FNR, HCHO,  $\text{NO}_2$ ,  $j\text{NO}_2$  (photolysis rates for  $\text{NO}_2 + h\nu$ ), and  $j\text{O}^1\text{D}$  (photolysis rates  
714 for  $\text{O}_3 + h\nu$ ). This parameterization demonstrated remarkable performance for the majority of air parcels  
715 collected in moderately to extremely polluted regions ( $\text{PO}_3 > 1$  ppbv/hr). However, it performed poorly in  
716 pristine regions due to the exclusion of certain significant ozone loss pathways, such as  $\text{HO}_x$  ( $\text{OH} + \text{HO}_2$ ),  
717 which are more challenging to predict.

718 Fortunately, TROPOMI provided critical data to enhance the representation of FNR, HCHO,  $\text{NO}_2$ ,  
719  $j\text{NO}_2$ , and  $j\text{O}^1\text{D}$ . We utilized TROPOMI's viewing geometry, UV surface albedo, and total ozone overhead  
720 from a model to predict  $j\text{NO}_2$  and  $j\text{O}^1\text{D}$  using look-up tables derived from NCAR's TUV model. To convert  
721 TROPOMI tropospheric  $\text{NO}_2$  and HCHO columns to their PBL mixing ratios, we employed the  
722 MERRA2GMI global transport model, extensively used in various studies. However, the coarse resolution  
723 of this model might have introduced underrepresentation issues, which could be mitigated by using higher  
724 spatial resolution models in future research.

725 To address the biases associated with TROPOMI observations, we updated comparisons from  
726 Verhoelst et al. (2021) and Vigouroux et al. (2020) with a larger dataset of paired TROPOMI and  
727 FTIR/MAX-DOAS measurements. TROPOMI retrievals significantly underestimated HCHO and  $\text{NO}_2$   
728 magnitudes in polluted regions (slope  $\sim 0.6 - 0.7$ ) and moderately overestimated them in pristine areas.  
729 These biases were corrected using regression lines, enabling a relatively unbiased application of the data.

730 To build confidence in our product, we propagated TROPOMI HCHO and  $\text{NO}_2$  errors to  $\text{PO}_3$   
731 estimates using a Monte Carlo approach. Results indicated that  $\text{PO}_3$  estimates were highly uncertain (100-  
732 300%) in clean regions due to a low trace gas signal in TROPOMI retrievals. However, in polluted regions,  
733 the errors were more moderate (40-60%) due to the stronger signal.

734 Over the years, extensive efforts have been devoted to measuring various critical atmospheric  
735 compounds globally, developing robust atmospheric models, and enhancing satellite retrievals along with  
736 their benchmarks. These advancements have enabled us to estimate  $\text{PO}_3$  maps within the planetary  
737 boundary layer (PBL) using comprehensive data. Nonetheless, it is crucial to acknowledge some limitations  
738 of our work, many of which are the focus of ongoing research within our team:



739 i) The direct measurement of  $\text{PO}_3$  using specialized instruments (Cazorla and Brune, 2010;  
740 Sadanaga et al., 2017; Sklaveniti et al., 2018) is lacking in most atmospheric composition datasets, limiting  
741 our ability to fully understand the effects of assumptions (such as the exclusion of heterogeneous chemistry)  
742 made in the box model on  $\text{PO}_3$ .

743 ii) There is potential for improvement in the parameterization process by employing more  
744 sophisticated algorithms, such as neural networks, which could increase the variance explained in the  
745 predicted  $\text{PO}_3$ .

746 iii) The conversion of satellite column data to PBL mixing ratios requires error characterization  
747 and the use of finer-resolution models that are comparable in size to the  $\text{PO}_3$  grid boxes.

748 iv) Partially cloudy pixels and aerosols can affect photolysis rates, which should be considered in  
749 future parameterization efforts.

750 Despite these limitations, our novel product offers an asset to the atmospheric science community.  
751 It provides a more comprehensive understanding of  $\text{PO}_3$ , sheds light on the complexities associated with  
752 spatiotemporal variability associated with the non-linear ozone chemistry at a large domain, enhances  
753 confidence in high-resolution maps of locally-produced ozone hotspots, and facilitates the investigation of  
754 disparities and inequalities in regions where environmental justice is a concern.

## 755 **Financial Support**

756 This study is funded by NASA's ACMAP project (grant no. 80NSSC23K1250). The measurements at  
757 Paramaribo have been supported by the BMBF (German Ministry of Education and Research) in project  
758 ROMIC-II's subproject TroStra (01LG1904A). The NDACC FTIR stations Bremen, Garmisch, Izaña, Ny-  
759 Ålesund, Paramaribo, and Karlsruhe have been supported by the German Bundesministerium für Wirtschaft  
760 und Energie (BMWi) via DLR5 under grants 50EE1711A, B, and D. The measurements and data analysis  
761 at Bremen are supported by the Senate of Bremen. The NCAR FTS observation programs at Thule, GR,  
762 Boulder, CO, and Mauna Loa, HI, are supported under contract by the National Aeronautics and Space  
763 Administration (NASA). The National Center for Atmospheric Research is sponsored by the National  
764 Science Foundation. The Thule effort is also supported by the NSF Office of Polar Programs (OPP).  
765 Operations at the Rikubetsu and Tsukuba FTIR sites are supported in part by the GOSAT series project. The  
766 Paris TCCON site has received funding from Sorbonne Université, the French research center CNRS, and  
767 the French space agency CNES. The Jungfraujoch FTIR data are primarily available thanks to the support  
768 provided by the F.R.S. FNRS (Brussels), the GAW-CH program of MeteoSwiss (Zürich), and the HFSJG.ch  
769 Foundation (Bern). IUP-Bremen ground-based measurements are funded by DLR-Bonn and received  
770 through project 50EE1709A. KNMI ground-based measurements in De Bilt and Cabauw are partly  
771 supported by the Ruisdael Observatory project, Dutch Research Council (NWO) contract 184.034.015, by  
772 the Netherlands Space Office (NSO) for Sentinel-5p/TROPOMI validation, and by ESA via the EU CAMS  
773 project.

## 774 **Competing interests**

775 Bryan N. Duncan is a member of the editorial board of Atmospheric Chemistry and Physics

## 776 **Acknowledgements**

777 We thank all principal investigators, pilots, and managers who collected the aircraft data used in our  
778 research and made them publicly available. We thank the FTIR HCHO measurement team of Thomas  
779 Blumenstock, Martine De Mazière, Michel Grutter, James W. Hannigan, Nicholas Jones, Rigel Kivi, Erik  
780 Lutsch, Emmanuel Mahieu, Maria Makarova, Isamu Morino, Isao Murata, Tomoo Nagahama, Justus





781 Notholt, Ivan Ortega, Mathias Palm, Amelie Röhlhng, Matthias Schneider, Dan Smale, Wolfgang Stremme,  
782 Kim String, Youwen Sun, Ralf Sussmann, Yao Té, and Pucai Wang. We thank the Meteorological Service  
783 Suriname and Cornelis Becker for their support. The MAX-DOAS data used in this publication were  
784 obtained from Alkis Bais, John Burrows, Ka Lok Chan, Michel Grutter, Cheng Liu, Hitoshi Irie, Vinod  
785 Kumar, Yugo Kanaya, Ankie Piters, Claudia Rivera-Cárdenas, Andreas Richter, Michel Van Roozendaal,  
786 Robert Ryan, Vinayak Sinha, and Thomas Wagner. Fast delivery of MAX-DOAS data tailored to the S5P  
787 validation was organized through S5PVT AO project NID-FORVAL. We thank the IISER Mohali  
788 atmospheric chemistry facility for supporting the MAX-DOAS measurements at Mohali, India. We thank  
789 Julie M. Nicely for providing merged ATOMs observations.

#### 790 **Authors' contributions**

791 AHS designed and implemented the research idea, analyzed the data, made all figures, and wrote the  
792 manuscript. TV, CV, GP, SC, and BL provided the paired TROPOMI and benchmark data. Other authors  
793 helped with the analysis, the model setup, and interpretation.

#### 794 **References:**

- 795 Ahamad, F., Griffiths, P. T., Latif, M. T., Juneng, L., and Xiang, C. J.: Ozone Trends from Two Decades of  
796 Ground Level Observation in Malaysia, *Atmosphere*, 11, 755,  
797 <https://doi.org/10.3390/atmos11070755>, 2020.
- 798 Anderson, D. C., Follette-Cook, M. B., Strode, S. A., Nicely, J. M., Liu, J., Ivatt, P. D., and Duncan, B.  
799 N.: A machine learning methodology for the generation of a parameterization of the hydroxyl radical,  
800 *Geosci. Model Dev.*, 15, 6341–6358, <https://doi.org/10.5194/gmd-15-6341-2022>, 2022.
- 801 Archibald, A. T., Jenkin, M. E., and Shallcross, D. E.: An isoprene mechanism intercomparison, *Atmos.*  
802 *Environ.*, 44, 5356–5364, <https://doi.org/10.1016/j.atmosenv.2009.09.016>, 2010.
- 803 Baylon, P., Jaffe, D. A., Hall, S. R., Ullmann, K., Alvarado, M. J., and Lefer, B. L.: Impact of Biomass  
804 Burning Plumes on Photolysis Rates and Ozone Formation at the Mount Bachelor Observatory, *J.*  
805 *Geophys. Res. Atmos.*, 123, 2272–2284, <https://doi.org/10.1002/2017JD027341>, 2018.
- 806 Beddows, D. C. S., Dall'Osto, M., and Harrison, R. M.: Cluster Analysis of Rural, Urban, and Curbside  
807 Atmospheric Particle Size Data, *Environ. Sci. Technol.*, 43, 4694–4700,  
808 <https://doi.org/10.1021/es803121t>, 2009.
- 809 Belhout, D., Kerbachi, R., Relvas, H., and Miranda, A. I.: Air quality assessment in Algiers city, *Air.*  
810 *Qual. Atmos. Health.*, 11, 897–906, <https://doi.org/10.1007/s11869-018-0589-x>, 2018.
- 811 Boraiy, M., El-Metwally, M., Wheida, A., El-Nazer, M., Hassan, S. K., El-Sanabary, F. F., Alfaro, S. C.,  
812 Abdelwahab, M., and Borbon, A.: Statistical analysis of the variability of reactive trace gases (SO<sub>2</sub>,  
813 NO<sub>2</sub> and ozone) in Greater Cairo during dust storm events, *J. Atmos. Chem.*, 80, 227–250,  
814 <https://doi.org/10.1007/s10874-023-09449-4>, 2023.
- 815 Botorff, B., Lew, M. M., Woo, Y., Rickly, P., Rollings, M. D., Deming, B., Anderson, D. C., Wood, E.,  
816 Alwe, H. D., Millet, D. B., Weinheimer, A., Tyndall, G., Ortega, J., Dusanter, S., Leonardis, T., Flynn,  
817 J., Erickson, M., Alvarez, S., Rivera-Rios, J. C., Shutter, J. D., Keutsch, F., Helmig, D., Wang, W.,  
818 Allen, H. M., Slade, J. H., Shepson, P. B., Bertman, S., and Stevens, P. S.: OH, HO<sub>2</sub>, and RO<sub>2</sub> radical  
819 chemistry in a rural forest environment: measurements, model comparisons, and evidence of a  
820 missing radical sink, *Atmos. Chem. Phys.*, 23, 10287–10311, [https://doi.org/10.5194/acp-23-10287-](https://doi.org/10.5194/acp-23-10287-2023)  
821 2023, 2023.





- 822 Brune, W. H., Miller, D. O., Thames, A. B., Allen, H. M., Apel, E. C., Blake, D. R., Bui, T. P., Commane,  
823 R., Crounse, J. D., Daube, B. C., Diskin, G. S., DiGangi, J. P., Elkins, J. W., Hall, S. R., Hanisco, T.  
824 F., Hannun, R. A., Hints, E. J., Hornbrook, R. S., Kim, M. J., McKain, K., Moore, F. L., Neuman, J.  
825 A., Nicely, J. M., Peischl, J., Ryerson, T. B., St. Clair, J. M., Sweeney, C., Teng, A. P., Thompson, C.,  
826 Ullmann, K., Veres, P. R., Wennberg, P. O., and Wolfe, G. M.: Exploring Oxidation in the Remote  
827 Free Troposphere: Insights From Atmospheric Tomography (ATom), *J. Geophys. Res. Atmos.*, 125,  
828 e2019JD031685, <https://doi.org/10.1029/2019JD031685>, 2020.
- 829 Brune, W. H., Miller, D. O., Thames, A. B., Brosius, A. L., Barletta, B., Blake, D. R., Blake, N. J., Chen,  
830 G., Choi, Y., Crawford, J. H., Digangi, J. P., Diskin, G., Fried, A., Hall, S. R., Hanisco, T. F., Huey, G.  
831 L., Hughes, S. C., Kim, M., Meinardi, S., Montzka, D. D., Pusede, S. E., Schroeder, J. R., Teng, A.,  
832 Tanner, D. J., Ullmann, K., Walega, J., Weinheimer, A., Wisthaler, A., and Wennberg, P. O.:  
833 Observations of atmospheric oxidation and ozone production in South Korea, *Atmos. Environ.*, 269,  
834 118854, <https://doi.org/10.1016/j.atmosenv.2021.118854>, 2022.
- 835 Cazorla, M. and Brune, W. H.: Measurement of Ozone Production Sensor, *Atmos. Meas. Tech.*, 3, 545–  
836 555, <https://doi.org/10.5194/amt-3-545-2010>, 2010.
- 837 Cazorla, M., Brune, W. H., Ren, X., and Lefter, B.: Direct measurement of ozone production rates in  
838 Houston in 2009 and comparison with two estimation methods, *Atmos. Chem. Phys.*, 12, 1203–1212,  
839 <https://doi.org/10.5194/acp-12-1203-2012>, 2012.
- 840 Chaichan, M. T., Kazem, H. A., and Abed, T. A.: Traffic and outdoor air pollution levels near highways in  
841 Baghdad, Iraq, *Environ. Dev. Sustain.*, 20, 589–603, <https://doi.org/10.1007/s10668-016-9900-x>,  
842 2018.
- 843 Chatfield, R. B., Ren, X., Brune, W., and Schwab, J.: Controls on urban ozone production rate as  
844 indicated by formaldehyde oxidation rate and nitric oxide, *Atmos. Environ.*, 44, 5395–5406,  
845 <https://doi.org/10.1016/j.atmosenv.2010.08.056>, 2010.
- 846 Choi, J., Henze, D. K., Cao, H., Nowlan, C. R., González Abad, G., Kwon, H.-A., Lee, H.-M., Oak, Y. J.,  
847 Park, R. J., Bates, K. H., Maasakkers, J. D., Wisthaler, A., and Weinheimer, A. J.: An Inversion  
848 Framework for Optimizing Non-Methane VOC Emissions Using Remote Sensing and Airborne  
849 Observations in Northeast Asia During the KORUS-AQ Field Campaign, *J. Geophys. Res. Atmos.*,  
850 127, e2021JD035844, <https://doi.org/10.1029/2021JD035844>, 2022.
- 851 Choi, S., Lamsal, L. N., Follette-Cook, M., Joiner, J., Krotkov, N. A., Swartz, W. H., Pickering, K. E.,  
852 Loughner, C. P., Appel, W., Pfister, G., Saide, P. E., Cohen, R. C., Weinheimer, A. J., and Herman, J.  
853 R.: Assessment of NO<sub>2</sub> observations during DISCOVER-AQ and KORUS-AQ field campaigns,  
854 *Atmos. Meas. Tech.*, 13, 2523–2546, <https://doi.org/10.5194/amt-13-2523-2020>, 2020.
- 855 Choi, Y. and Souri, A. H.: Chemical condition and surface ozone in large cities of Texas during the last  
856 decade: Observational evidence from OMI, CAMS, and model analysis, *Remote Sens. Environ.*, 168,  
857 90–101, <https://doi.org/10.1016/j.rse.2015.06.026>, 2015a.
- 858 Choi, Y. and Souri, A. H.: Seasonal behavior and long-term trends of tropospheric ozone, its precursors  
859 and chemical conditions over Iran: A view from space, *Atmos. Environ.*, 106, 232–240,  
860 <https://doi.org/10.1016/j.atmosenv.2015.02.012>, 2015b.
- 861 Choi, Y., Kim, H., Tong, D., and Lee, P.: Summertime weekly cycles of observed and modeled NO<sub>x</sub> and  
862 O<sub>3</sub> concentrations as a function of satellite-derived ozone production sensitivity and land use types  
863 over the Continental United States, *Atmos. Chem. Phys.*, 12, 6291–6307, <https://doi.org/10.5194/acp-12-6291-2012>, 2012.



- 865 Colombi, N. K., Jacob, D. J., Yang, L. H., Zhai, S., Shah, V., Grange, S. K., Yantosca, R. M., Kim, S., and  
866 Liao, H.: Why is ozone in South Korea and the Seoul metropolitan area so high and increasing?,  
867 *Atmos. Chem. Phys.*, 23, 4031–4044, <https://doi.org/10.5194/acp-23-4031-2023>, 2023.
- 868 Crawford, J. H., Ahn, J.-Y., Al-Saadi, J., Chang, L., Emmons, L. K., Kim, J., Lee, G., Park, J.-H., Park, R.  
869 J., Woo, J. H., Song, C.-K., Hong, J.-H., Hong, Y.-D., Lefer, B. L., Lee, M., Lee, T., Kim, S., Min, K.-  
870 E., Yum, S. S., Shin, H. J., Kim, Y.-W., Choi, J.-S., Park, J.-S., Szykman, J. J., Long, R. W., Jordan, C.  
871 E., Simpson, I. J., Fried, A., Dibb, J. E., Cho, S., and Kim, Y. P.: The Korea–United States Air Quality  
872 (KORUS-AQ) field study, *Elem. Sci. Anth.*, 9, 00163, <https://doi.org/10.1525/elementa.2020.00163>,  
873 2021.
- 874 De Smedt, I., Pinardi, G., Vigouroux, C., Compornolle, S., Bais, A., Benavent, N., Boersma, F., Chan, K.-  
875 L., Donner, S., Eichmann, K.-U., Hedelt, P., Hendrick, F., Irie, H., Kumar, V., Lambert, J.-C.,  
876 Langerock, B., Lerot, C., Liu, C., Loyola, D., PETERS, A., Richter, A., Rivera Cárdenas, C., Romahn, F.,  
877 Ryan, R. G., Sinha, V., Theys, N., Vlietinck, J., Wagner, T., Wang, T., Yu, H., and Van Roozendael,  
878 M.: Comparative assessment of TROPOMI and OMI formaldehyde observations and validation  
879 against MAX-DOAS network column measurements, *Atmos. Chem. Phys.*, 21, 12561–12593,  
880 <https://doi.org/10.5194/acp-21-12561-2021>, 2021.
- 881 DiMaria, C. A., Jones, D. B. A., Worden, H., Bloom, A. A., Bowman, K., Stavrou, T., Miyazaki, K.,  
882 Worden, J., Guenther, A., Sarkar, C., Seco, R., Park, J.-H., Tota, J., Alves, E. G., and Ferracci, V.:  
883 Optimizing the Isoprene Emission Model MEGAN With Satellite and Ground-Based Observational  
884 Constraints, *J. Geophys. Res. Atmos.*, 128, e2022JD037822, <https://doi.org/10.1029/2022JD037822>,  
885 2023.
- 886 Duncan, B. N. and Chameides, W. L.: Effects of urban emission control strategies on the export of ozone  
887 and ozone precursors from the urban atmosphere to the troposphere, *J. Geophys. Res. Atmos.*, 103,  
888 28159–28179, <https://doi.org/10.1029/98JD02145>, 1998.
- 889 Duncan, B. N., Strahan, S. E., Yoshida, Y., Steenrod, S. D., and Livesey, N.: Model study of the cross-  
890 tropopause transport of biomass burning pollution, *Atmos. Chem. Phys.*, 7, 3713–3736,  
891 <https://doi.org/10.5194/acp-7-3713-2007>, 2007.
- 892 Duncan, B. N., Yoshida, Y., Olson, J. R., Sillman, S., Martin, R. V., Lamsal, L., Hu, Y., Pickering, K. E.,  
893 Retscher, C., Allen, D. J., and Crawford, J. H.: Application of OMI observations to a space-based  
894 indicator of NO<sub>x</sub> and VOC controls on surface ozone formation, *Atmos. Environ.*, 44, 2213–2223,  
895 <https://doi.org/10.1016/j.atmosenv.2010.03.010>, 2010.
- 896 van Geffen, J., Eskes, H., Compornolle, S., Pinardi, G., Verhoelst, T., Lambert, J.-C., Sneep, M., ter  
897 Linden, M., Ludewig, A., Boersma, K. F., and Veeffkind, J. P.: Sentinel-5P TROPOMI NO<sub>2</sub> retrieval:  
898 impact of version v2.2 improvements and comparisons with OMI and ground-based data, *Atmos.*  
899 *Meas. Tech.*, 15, 2037–2060, <https://doi.org/10.5194/amt-15-2037-2022>, 2022.
- 900 Gerasopoulos, E., Kouvarakis, G., Vrekoussis, M., Donoussis, C., Mihalopoulos, N., and Kanakidou, M.:  
901 Photochemical ozone production in the Eastern Mediterranean, *Atmos. Environ.*, 40, 3057–3069,  
902 <https://doi.org/10.1016/j.atmosenv.2005.12.061>, 2006.
- 903 Govender, P. and Sivakumar, V.: Application of k-means and hierarchical clustering techniques for  
904 analysis of air pollution: A review (1980–2019), *Atmos. Pollut. Res.*, 11, 40–56,  
905 <https://doi.org/10.1016/j.apr.2019.09.009>, 2020.
- 906 Jeon, W., Choi, Y., Souri, A. H., Roy, A., Diao, L., Pan, S., Lee, H. W., and Lee, S.-H.: Identification of  
907 chemical fingerprints in long-range transport of burning induced upper tropospheric ozone from



- 908 Colorado to the North Atlantic Ocean, *Sci. Total Environ.*, 613–614, 820–828,  
909 <https://doi.org/10.1016/j.scitotenv.2017.09.177>, 2018.
- 910 Jin, X., Fiore, A. M., Murray, L. T., Valin, L. C., Lamsal, L. N., Duncan, B., Folkert Boersma, K., De  
911 Smedt, I., Abad, G. G., Chance, K., and Tonnesen, G. S.: Evaluating a Space-Based Indicator of  
912 Surface Ozone-NO<sub>x</sub>-VOC Sensitivity Over Midlatitude Source Regions and Application to Decadal  
913 Trends, *J. Geophys. Res. Atmos.*, 122, 10,439–10,461, <https://doi.org/10.1002/2017JD026720>, 2017.
- 914 Johnson, M. S., Souri, A. H., Philip, S., Kumar, R., Naeger, A., Geddes, J., Judd, L., Janz, S., Chong, H.,  
915 and Sullivan, J.: Satellite remote-sensing capability to assess tropospheric-column ratios of  
916 formaldehyde and nitrogen dioxide: case study during the Long Island Sound Tropospheric Ozone  
917 Study 2018 (LISTOS 2018) field campaign, *Atmos. Meas. Tech.*, 16, 2431–2454,  
918 <https://doi.org/10.5194/amt-16-2431-2023>, 2023.
- 919 Kim, S.-W., McDonald, B. C., Seo, S., Kim, K.-M., and Trainer, M.: Understanding the Paths of Surface  
920 Ozone Abatement in the Los Angeles Basin, *J. Geophys. Res. Atmos.*, 127, e2021JD035606,  
921 <https://doi.org/10.1029/2021JD035606>, 2022.
- 922 Kleinman, L. I., Daum, P. H., Imre, D., Lee, Y.-N., Nunnermacker, L. J., Springston, S. R., Weinstein-  
923 Lloyd, J., and Rudolph, J.: Ozone production rate and hydrocarbon reactivity in 5 urban areas: A  
924 cause of high ozone concentration in Houston, *Geophys. Res. Lett.*, 29, 105-1-105-4,  
925 <https://doi.org/10.1029/2001GL014569>, 2002.
- 926 Kusumaningtyas, S. D. A., Tonokura, K., Muharsyah, R., Gunawan, D., Sopaheluwakan, A., Iriana, W.,  
927 Lestari, P., Permadi, D. A., Rahmawati, R., and Samputra, N. A. R.: Comprehensive analysis of long-  
928 term trends, meteorological influences, and ozone formation sensitivity in the Jakarta Greater Area,  
929 *Sci. Rep.*, 14, 9605, <https://doi.org/10.1038/s41598-024-60374-2>, 2024.
- 930 Lelieveld, J., Hoor, P., Jöckel, P., Pozzer, A., Hadjinicolaou, P., Cammas, J.-P., and Beirle, S.: Severe  
931 ozone air pollution in the Persian Gulf region, *Atmos. Chem. Phys.*, 9, 1393–1406,  
932 <https://doi.org/10.5194/acp-9-1393-2009>, 2009.
- 933 Li, K., Jacob, D. J., Liao, H., Shen, L., Zhang, Q., and Bates, K. H.: Anthropogenic drivers of 2013–2017  
934 trends in summer surface ozone in China, *Proc. Natl. Acad. Sci.*, 116, 422–427,  
935 <https://doi.org/10.1073/pnas.1812168116>, 2019.
- 936 Marais, E. A., Jacob, D. J., Guenther, A., Chance, K., Kurosu, T. P., Murphy, J. G., Reeves, C. E., and  
937 Pye, H. O. T.: Improved model of isoprene emissions in Africa using Ozone Monitoring Instrument  
938 (OMI) satellite observations of formaldehyde: implications for oxidants and particulate matter,  
939 *Atmos. Chem. Phys.*, 14, 7693–7703, <https://doi.org/10.5194/acp-14-7693-2014>, 2014.
- 940 Martin, R. V., Fiore, A. M., and Van Donkelaar, A.: Space-based diagnosis of surface ozone sensitivity to  
941 anthropogenic emissions, *Geophys. Res. Lett.*, 31, <https://doi.org/10.1029/2004GL019416>, 2004.
- 942 Marvin, M. R., Wolfe, G. M., Salawitch, R. J., Canty, T. P., Roberts, S. J., Travis, K. R., Aikin, K. C., de  
943 Gouw, J. A., Graus, M., Hanisco, T. F., Holloway, J. S., Hübler, G., Kaiser, J., Keutsch, F. N., Peischl,  
944 J., Pollack, I. B., Roberts, J. M., Ryerson, T. B., Veres, P. R., and Warneke, C.: Impact of evolving  
945 isoprene mechanisms on simulated formaldehyde: An inter-comparison supported by in situ  
946 observations from SENEX, *Atmos. Environ.*, 164, 325–336,  
947 <https://doi.org/10.1016/j.atmosenv.2017.05.049>, 2017.
- 948 Mazzuca, G. M., Ren, X., Loughner, C. P., Estes, M., Crawford, J. H., Pickering, K. E., Weinheimer, A. J.,  
949 and Dickerson, R. R.: Ozone production and its sensitivity to NO<sub>x</sub> and VOCs: results from the  
950 DISCOVER-AQ field experiment, Houston 2013, *Atmos. Chem. Phys.*, 16, 14463–14474,  
951 <https://doi.org/10.5194/acp-16-14463-2016>, 2016.



- 952 Miller, D. O. and Brune, W. H.: Investigating the Understanding of Oxidation Chemistry Using 20 Years  
953 of Airborne OH and HO<sub>2</sub> Observations, *J. Geophys. Res. Atmos.*, 127, e2021JD035368,  
954 <https://doi.org/10.1029/2021JD035368>, 2022.
- 955 Miyazaki, K., Eskes, H., Sudo, K., Boersma, K. F., Bowman, K., and Kanaya, Y.: Decadal changes in  
956 global surface NO<sub>x</sub> emissions from multi-constituent satellite data assimilation, *Atmos. Chem. Phys.*,  
957 17, 807–837, <https://doi.org/10.5194/acp-17-807-2017>, 2017.
- 958 Orbe, C., Oman, L. D., Strahan, S. E., Waugh, D. W., Pawson, S., Takacs, L. L., and Molod, A. M.: Large-  
959 Scale Atmospheric Transport in GEOS Replay Simulations, *J. Adv. Model. Earth Syst.*, 9, 2545–2560,  
960 <https://doi.org/10.1002/2017MS001053>, 2017.
- 961 Pan, S., Roy, A., Choi, Y., Eslami, E., Thomas, S., Jiang, X., and Gao, H. O.: Potential impacts of electric  
962 vehicles on air quality and health endpoints in the Greater Houston Area in 2040, *Atmos. Environ.*,  
963 207, 38–51, <https://doi.org/10.1016/j.atmosenv.2019.03.022>, 2019.
- 964 Ren, X., van Duin, D., Cazorla, M., Chen, S., Mao, J., Zhang, L., Brune, W. H., Flynn, J. H., Grossberg,  
965 N., Lefer, B. L., Rappenglück, B., Wong, K. W., Tsai, C., Stutz, J., Dibb, J. E., Thomas Jobson, B.,  
966 Luke, W. T., and Kelley, P.: Atmospheric oxidation chemistry and ozone production: Results from  
967 SHARP 2009 in Houston, Texas, *J. Geophys. Res. Atmos.*, 118, 5770–5780,  
968 <https://doi.org/10.1002/jgrd.50342>, 2013.
- 969 Roberts, G., Wooster, M. J., and Lagoudakis, E.: Annual and diurnal african biomass burning temporal  
970 dynamics, *Biogeosciences*, 6, 849–866, <https://doi.org/10.5194/bg-6-849-2009>, 2009.
- 971 Sadanaga, Y., Kawasaki, S., Tanaka, Y., Kajii, Y., and Bandow, H.: New System for Measuring the  
972 Photochemical Ozone Production Rate in the Atmosphere, *Environ. Sci. Technol.*, 51, 2871–2878,  
973 <https://doi.org/10.1021/acs.est.6b04639>, 2017.
- 974 Sakamoto, Y., Shoji, K., Bui, M. T., Pham, T. H., Vu, T. A., Ly, B. T., and Kajii, Y.: Air quality study in  
975 Hanoi, Vietnam in 2015–2016 based on a one-year observation of NO<sub>x</sub>, O<sub>3</sub>, CO and a one-week  
976 observation of VOCs, *Atmos. Pollut. Res.*, 9, 544–551, <https://doi.org/10.1016/j.apr.2017.12.001>,  
977 2018.
- 978 Schroeder, J. R., Crawford, J. H., Fried, A., Walega, J., Weinheimer, A., Wisthaler, A., Müller, M.,  
979 Mikoviny, T., Chen, G., Shook, M., Blake, D. R., and Tonnesen, G. S.: New insights into the column  
980 CH<sub>2</sub>O/NO<sub>2</sub> ratio as an indicator of near-surface ozone sensitivity, *J. Geophys. Res. Atmos.*, 122,  
981 8885–8907, <https://doi.org/10.1002/2017JD026781>, 2017.
- 982 Schroeder, J. R., Crawford, J. H., Ahn, J.-Y., Chang, L., Fried, A., Walega, J., Weinheimer, A., Montzka,  
983 D. D., Hall, S. R., Ullmann, K., Wisthaler, A., Mikoviny, T., Chen, G., Blake, D. R., Blake, N. J.,  
984 Hughes, S. C., Meinardi, S., Diskin, G., Digangi, J. P., Choi, Y., Pusede, S. E., Huey, G. L., Tanner, D.  
985 J., Kim, M., and Wennberg, P.: Observation-based modeling of ozone chemistry in the Seoul  
986 metropolitan area during the Korea-United States Air Quality Study (KORUS-AQ), *Elem. Sci. Anth.*,  
987 8, 3, <https://doi.org/10.1525/elementa.400>, 2020.
- 988 Sillman, S. and He, D.: Some theoretical results concerning O<sub>3</sub>-NO<sub>x</sub>-VOC chemistry and NO<sub>x</sub>-VOC  
989 indicators, *J. Geophys. Res. Atmos.*, 107, ACH 26-1-ACH 26-15,  
990 <https://doi.org/10.1029/2001JD001123>, 2002.
- 991 Silva, S. J., Heald, C. L., Ravela, S., Mammarella, I., and Munger, J. W.: A Deep Learning  
992 Parameterization for Ozone Dry Deposition Velocities, *Geophys. Res. Lett.*, 46, 983–989,  
993 <https://doi.org/10.1029/2018GL081049>, 2019.





- 994 Simpson, W. R., Brown, S. S., Saiz-Lopez, A., Thornton, J. A., and von Glasow, R.: Tropospheric  
995 Halogen Chemistry: Sources, Cycling, and Impacts, *Chem. Rev.*, 115, 4035–4062,  
996 <https://doi.org/10.1021/cr5006638>, 2015.
- 997 Singh, H. B., Brune, W. H., Crawford, J. H., Flocke, F., and Jacob, D. J.: Chemistry and transport of  
998 pollution over the Gulf of Mexico and the Pacific: spring 2006 INTEX-B campaign overview and  
999 first results, *Atmos. Chem. Phys.*, 9, 2301–2318, <https://doi.org/10.5194/acp-9-2301-2009>, 2009.
- 1000 Sklaventini, S., Locoge, N., Stevens, P. S., Wood, E., Kundu, S., and Dusanter, S.: Development of an  
1001 instrument for direct ozone production rate measurements: measurement reliability and current  
1002 limitations, *Atmos. Meas. Tech.*, 11, 741–761, <https://doi.org/10.5194/amt-11-741-2018>, 2018.
- 1003 Souri, A. H., Choi, Y., Li, X., Kotsakis, A., and Jiang, X.: A 15-year climatology of wind pattern impacts  
1004 on surface ozone in Houston, Texas, *Atmos. Res.*, 174–175, 124–134,  
1005 <https://doi.org/10.1016/j.atmosres.2016.02.007>, 2016b.
- 1006 Souri, A. H., Choi, Y., Jeon, W., Li, X., Pan, S., Diao, L., and Westenbarger, D. A.: Constraining NO<sub>x</sub>  
1007 emissions using satellite NO<sub>2</sub> measurements during 2013 DISCOVER-AQ Texas campaign, *Atmos.*  
1008 *Environ.*, 131, 371–381, <https://doi.org/10.1016/j.atmosenv.2016.02.020>, 2016a.
- 1009 Souri, A. H., Nowlan, C. R., González Abad, G., Zhu, L., Blake, D. R., Fried, A., Weinheimer, A. J.,  
1010 Wisthaler, A., Woo, J.-H., Zhang, Q., Chan Miller, C. E., Liu, X., and Chance, K.: An inversion of  
1011 NO<sub>x</sub> and non-methane volatile organic compound (NMVOC) emissions using satellite observations  
1012 during the KORUS-AQ campaign and implications for surface ozone over East Asia, *Atmos. Chem.*  
1013 *Phys.*, 20, 9837–9854, <https://doi.org/10.5194/acp-20-9837-2020>, 2020b.
- 1014 Souri, A. H., Nowlan, C. R., Wolfe, G. M., Lamsal, L. N., Chan Miller, C. E., Abad, G. G., Janz, S. J.,  
1015 Fried, A., Blake, D. R., Weinheimer, A. J., Diskin, G. S., Liu, X., and Chance, K.: Revisiting the  
1016 effectiveness of HCHO/NO<sub>2</sub> ratios for inferring ozone sensitivity to its precursors using high  
1017 resolution airborne remote sensing observations in a high ozone episode during the KORUS-AQ  
1018 campaign, *Atmos. Environ.*, 224, 117341, <https://doi.org/10.1016/j.atmosenv.2020.117341>, 2020a.
- 1019 Souri, A. H., Chance, K., Bak, J., Nowlan, C. R., González Abad, G., Jung, Y., Wong, D. C., Mao, J., and  
1020 Liu, X.: Unraveling pathways of elevated ozone induced by the 2020 lockdown in Europe by an  
1021 observationally constrained regional model using TROPOMI, *Atmos. Chem. Phys.*, 21, 18227–18245,  
1022 <https://doi.org/10.5194/acp-21-18227-2021>, 2021.
- 1023 Souri, A. H., Johnson, M. S., Wolfe, G. M., Crawford, J. H., Fried, A., Wisthaler, A., Brune, W. H., Blake,  
1024 D. R., Weinheimer, A. J., Verhoelst, T., Compernelle, S., Pinardi, G., Vigouroux, C., Langerock, B.,  
1025 Choi, S., Lamsal, L., Zhu, L., Sun, S., Cohen, R. C., Min, K.-E., Cho, C., Philip, S., Liu, X., and  
1026 Chance, K.: Characterization of errors in satellite-based HCHO/NO<sub>2</sub> tropospheric column ratios with  
1027 respect to chemistry, column-to-PBL translation, spatial representation, and retrieval uncertainties,  
1028 *Atmos. Chem. Phys.*, 23, 1963–1986, <https://doi.org/10.5194/acp-23-1963-2023>, 2023.
- 1029 Souri, A. H., Duncan, B. N., Strode, S. A., Anderson, D. C., Manyin, M. E., Liu, J., Oman, L. D., Zhang,  
1030 Z., and Weir, B.: Enhancing Long-Term Trend Simulation of Global Tropospheric OH and Its Drivers  
1031 from 2005-2019: A Synergistic Integration of Model Simulations and Satellite Observations,  
1032 *EGUsphere*, 1–37, <https://doi.org/10.5194/egusphere-2024-410>, 2024.
- 1033 Stanier, C. O., Pierce, R. B., Abdi-Oskouei, M., Adelman, Z. E., Al-Saadi, J., Alwe, H. D., Bertram, T. H.,  
1034 Carmichael, G. R., Christiansen, M. B., Cleary, P. A., Czarnetzki, A. C., Dickens, A. F., Fuoco, M. A.,  
1035 Hughes, D. D., Hupy, J. P., Janz, S. J., Judd, L. M., Kenski, D., Kowalewski, M. G., Long, R. W.,  
1036 Millet, D. B., Novak, G., Roozitalab, B., Shaw, S. L., Stone, E. A., Szykman, J., Valin, L., Vermeuel,  
1037 M., Wagner, T. J., Whitehill, A. R., and Williams, D. J.: Overview of the Lake Michigan Ozone Study



- 1038 2017, *Bull. Am. Meteorol. Soc.*, 102, E2207–E2225, <https://doi.org/10.1175/BAMS-D-20-0061.1>,  
1039 2021.
- 1040 Stavroukou, T., Müller, J.-F., Bauwens, M., De Smedt, I., Lerot, C., Van Roozendaal, M., Coheur, P.-F.,  
1041 Clerbaux, C., Boersma, K. F., van der A, R., and Song, Y.: Substantial Underestimation of Post-  
1042 Harvest Burning Emissions in the North China Plain Revealed by Multi-Species Space Observations,  
1043 *Sci. Rep.*, 6, 32307, <https://doi.org/10.1038/srep32307>, 2016.
- 1044 Strode, S. A., Ziemke, J. R., Oman, L. D., Lamsal, L. N., Olsen, M. A., and Liu, J.: Global changes in the  
1045 diurnal cycle of surface ozone, *Atmos. Environ.*, 199, 323–333,  
1046 <https://doi.org/10.1016/j.atmosenv.2018.11.028>, 2019.
- 1047 Tao, M., Fiore, A. M., Jin, X., Schiferl, L. D., Commane, R., Judd, L. M., Janz, S., Sullivan, J. T., Miller,  
1048 P. J., Karambelas, A., Davis, S., Tzortziou, M., Valin, L., Whitehill, A., Civerolo, K., and Tian, Y.:  
1049 Investigating Changes in Ozone Formation Chemistry during Summertime Pollution Events over the  
1050 Northeastern United States, *Environ. Sci. Technol.*, 56, 15312–15327,  
1051 <https://doi.org/10.1021/acs.est.2c02972>, 2022.
- 1052 Thompson, A. M., Balashov, N. V., Witte, J. C., Coetzee, J. G. R., Thouret, V., and Posny, F.:  
1053 Tropospheric ozone increases over the southern Africa region: bellwether for rapid growth in  
1054 Southern Hemisphere pollution?, *Atmos. Chem. Phys.*, 14, 9855–9869, <https://doi.org/10.5194/acp-14-9855-2014>, 2014.
- 1056 Thompson, C. R., Wofsy, S. C., Prather, M. J., Newman, P. A., Hanisco, T. F., Ryerson, T. B., Fahey, D.  
1057 W., Apel, E. C., Brock, C. A., Brune, W. H., Froyd, K., Katich, J. M., Nicely, J. M., Peischl, J., Ray,  
1058 E., Veres, P. R., Wang, S., Allen, H. M., Asher, E., Bian, H., Blake, D., Bourgeois, I., Budney, J., Bui,  
1059 T. P., Butler, A., Campuzano-Jost, P., Chang, C., Chin, M., Commane, R., Correa, G., Crouse, J. D.,  
1060 Daube, B., Dibb, J. E., DiGangi, J. P., Diskin, G. S., Dollner, M., Elkins, J. W., Fiore, A. M., Flynn, C.  
1061 M., Guo, H., Hall, S. R., Hannun, R. A., Hills, A., Hintsa, E. J., Hodzic, A., Hornbrook, R. S., Huey,  
1062 L. G., Jimenez, J. L., Keeling, R. F., Kim, M. J., Kupc, A., Lacey, F., Lait, L. R., Lamarque, J.-F., Liu,  
1063 J., McKain, K., Meinardi, S., Miller, D. O., Montzka, S. A., Moore, F. L., Morgan, E. J., Murphy, D.  
1064 M., Murray, L. T., Nault, B. A., Neuman, J. A., Nguyen, L., González, Y., Rollins, A., Rosenlof, K.,  
1065 Sargent, M., Schill, G., Schwarz, J. P., Clair, J. M. S., Steenrod, S. D., Stephens, B. B., Strahan, S. E.,  
1066 Strode, S. A., Sweeney, C., Thames, A. B., Ullmann, K., Wagner, N., Weber, R., Weinzierl, B.,  
1067 Wennberg, P. O., Williamson, C. J., Wolfe, G. M., and Zeng, L.: The NASA Atmospheric  
1068 Tomography (ATOM) Mission: Imaging the Chemistry of the Global Atmosphere, *Bull. Am. Meteorol.*  
1069 *Soc.*, 103, E761–E790, <https://doi.org/10.1175/BAMS-D-20-0315.1>, 2022.
- 1070 Thornton, J. A., Wooldridge, P. J., Cohen, R. C., Martinez, M., Harder, H., Brune, W. H., Williams, E. J.,  
1071 Roberts, J. M., Fehsenfeld, F. C., Hall, S. R., Shetter, R. E., Wert, B. P., and Fried, A.: Ozone  
1072 production rates as a function of NO<sub>x</sub> abundances and HO<sub>x</sub> production rates in the Nashville urban  
1073 plume, *J. Geophys. Res. Atmos.*, 107, ACH 7-1-ACH 7-17, <https://doi.org/10.1029/2001JD000932>,  
1074 2002.
- 1075 Tibshirani, R.: Regression Shrinkage and Selection via the Lasso, *J. R. Stat. B (Methodological)*, 58, 267–  
1076 288, 1996.
- 1077 Tilstra, L. G., de Graaf, M., Trees, V., Litvinov, P., Dubovik, O., and Stammes, P.: A directional surface  
1078 reflectance climatology determined from TROPOMI observations, *Atmos. Meas. Tech. Discussions*,  
1079 1–29, <https://doi.org/10.5194/amt-2023-222>, 2023.
- 1080 Tonnesen, G. S. and Dennis, R. L.: Analysis of radical propagation efficiency to assess ozone sensitivity  
1081 to hydrocarbons and NO<sub>x</sub>: 1. Local indicators of instantaneous odd oxygen production sensitivity, *J.*  
1082 *Geophys. Res.*, 105, 9213–9225, <https://doi.org/10.1029/1999JD900371>, 2000a.



- 1083 Tonnesen, G. S. and Dennis, R. L.: Analysis of radical propagation efficiency to assess ozone sensitivity  
1084 to hydrocarbons and NO<sub>x</sub>: 2. Long-lived species as indicators of ozone concentration sensitivity, *J.*  
1085 *Geophys. Res.*, 105, 9227–9241, <https://doi.org/10.1029/1999JD900372>, 2000b.
- 1086 Veefkind, J. P., Aben, I., McMullan, K., Förster, H., de Vries, J., Otter, G., Claas, J., Eskes, H. J., de Haan,  
1087 J. F., Kleipool, Q., van Weele, M., Hasekamp, O., Hoogeveen, R., Landgraf, J., Snel, R., Tol, P.,  
1088 Ingmann, P., Voors, R., Kruizinga, B., Vink, R., Visser, H., and Levelt, P. F.: TROPOMI on the ESA  
1089 Sentinel-5 Precursor: A GMES mission for global observations of the atmospheric composition for  
1090 climate, air quality and ozone layer applications, *Remote Sens. Environ.*, 120, 70–83,  
1091 <https://doi.org/10.1016/j.rse.2011.09.027>, 2012.
- 1092 van der Velde, I. R., van der Werf, G. R., Houweling, S., Eskes, H. J., Veefkind, J. P., Borsdorff, T., and  
1093 Aben, I.: Biomass burning combustion efficiency observed from space using measurements of CO  
1094 and NO<sub>2</sub> by the TROPospheric Monitoring Instrument (TROPOMI), *Atmos. Chem. Phys.*, 21, 597–  
1095 616, <https://doi.org/10.5194/acp-21-597-2021>, 2021.
- 1096 Verhoelst, T., Compernelle, S., Pinardi, G., Lambert, J.-C., Eskes, H. J., Eichmann, K.-U., Fjæraa, A. M.,  
1097 Granville, J., Niemeijer, S., Cede, A., Tiefengraber, M., Hendrick, F., Pazmiño, A., Bais, A.,  
1098 Bazureau, A., Boersma, K. F., Bogner, K., Dehn, A., Donner, S., Elokhov, A., Gebetsberger, M.,  
1099 Goutail, F., Grutter de la Mora, M., Gruzdev, A., Gratsea, M., Hansen, G. H., Irie, H., Jepsen, N.,  
1100 Kanaya, Y., Karagkiozidis, D., Kivi, R., Kreher, K., Levelt, P. F., Liu, C., Müller, M., Navarro Comas,  
1101 M., Piters, A. J. M., Pommereau, J.-P., Portafaix, T., Prados-Roman, C., Puentedura, O., Querel, R.,  
1102 Remmers, J., Richter, A., Rimmer, J., Rivera Cárdenas, C., Saavedra de Miguel, L., Sinyakov, V. P.,  
1103 Stremme, W., Strong, K., Van Roozendaal, M., Veefkind, J. P., Wagner, T., Wittrock, F., Yela  
1104 González, M., and Zehner, C.: Ground-based validation of the Copernicus Sentinel-5P TROPOMI  
1105 NO<sub>2</sub> measurements with the NDACC ZSL-DOAS, MAX-DOAS and Pandonia global networks,  
1106 *Atmos. Meas. Tech.*, 14, 481–510, <https://doi.org/10.5194/amt-14-481-2021>, 2021.
- 1107 Vigouroux, C., Langerock, B., Bauer Aquino, C. A., Blumenstock, T., Cheng, Z., De Mazière, M., De  
1108 Smedt, I., Grutter, M., Hannigan, J. W., Jones, N., Kivi, R., Loyola, D., Lutsch, E., Mahieu, E.,  
1109 Makarova, M., Metzger, J.-M., Morino, I., Murata, I., Nagahama, T., Notholt, J., Ortega, I., Palm, M.,  
1110 Pinardi, G., Röhlings, A., Smale, D., Stremme, W., Strong, K., Sussmann, R., Té, Y., van Roozendaal,  
1111 M., Wang, P., and Winkler, H.: TROPOMI–Sentinel-5 Precursor formaldehyde validation using an  
1112 extensive network of ground-based Fourier-transform infrared stations, *Atmos. Meas. Tech.*, 13,  
1113 3751–3767, <https://doi.org/10.5194/amt-13-3751-2020>, 2020.
- 1114 Wang, T., Xue, L., Brimblecombe, P., Lam, Y. F., Li, L., and Zhang, L.: Ozone pollution in China: A  
1115 review of concentrations, meteorological influences, chemical precursors, and effects, *Sci. Total*  
1116 *Environ.*, 575, 1582–1596, <https://doi.org/10.1016/j.scitotenv.2016.10.081>, 2017.
- 1117 Wang, W., Parrish, D. D., Li, X., Shao, M., Liu, Y., Mo, Z., Lu, S., Hu, M., Fang, X., Wu, Y., Zeng, L.,  
1118 and Zhang, Y.: Exploring the drivers of the increased ozone production in Beijing in summertime  
1119 during 2005–2016, *Atmos. Chem. Phys.*, 20, 15617–15633, [https://doi.org/10.5194/acp-20-15617-](https://doi.org/10.5194/acp-20-15617-2020)  
1120 2020, 2020.
- 1121 Warneke, C., Trainer, M., de Gouw, J. A., Parrish, D. D., Fahey, D. W., Ravishankara, A. R., Middlebrook,  
1122 A. M., Brock, C. A., Roberts, J. M., Brown, S. S., Neuman, J. A., Lerner, B. M., Lack, D., Law, D.,  
1123 Hübler, G., Pollack, I., Sjostedt, S., Ryerson, T. B., Gilman, J. B., Liao, J., Holloway, J., Peischl, J.,  
1124 Nowak, J. B., Aikin, K. C., Min, K.-E., Washenfelder, R. A., Graus, M. G., Richardson, M.,  
1125 Markovic, M. Z., Wagner, N. L., Welti, A., Veres, P. R., Edwards, P., Schwarz, J. P., Gordon, T., Dube,  
1126 W. P., McKeen, S. A., Brioude, J., Ahmadov, R., Bougiatioti, A., Lin, J. J., Nenes, A., Wolfe, G. M.,  
1127 Hanisco, T. F., Lee, B. H., Lopez-Hilfiker, F. D., Thornton, J. A., Keutsch, F. N., Kaiser, J., Mao, J.,  
1128 and Hatch, C. D.: Instrumentation and measurement strategy for the NOAA SENEX aircraft



- 1129 campaign as part of the Southeast Atmosphere Study 2013, *Atmos. Meas. Tech.*, 9, 3063–3093,  
1130 <https://doi.org/10.5194/amt-9-3063-2016>, 2016.
- 1131 Wolfe, G. M., Marvin, M. R., Roberts, S. J., Travis, K. R., and Liao, J.: The Framework for 0-D  
1132 Atmospheric Modeling (F0AM) v3.1, *Geosci. Model Dev.*, 9, 3309–3319,  
1133 <https://doi.org/10.5194/gmd-9-3309-2016>, 2016.
- 1134 Wolfe, G. M., Hanisco, T. F., Arkinson, H. L., Blake, D. R., Wisthaler, A., Mikoviny, T., Ryerson, T. B.,  
1135 Pollack, I., Peischl, J., Wennberg, P. O., Crouse, J. D., St. Clair, J. M., Teng, A., Huey, L. G., Liu, X.,  
1136 Fried, A., Weibring, P., Richter, D., Walega, J., Hall, S. R., Ullmann, K., Jimenez, J. L., Campuzano-  
1137 Jost, P., Bui, T. P., Diskin, G., Podolske, J. R., Sachse, G., and Cohen, R. C.: Photochemical evolution  
1138 of the 2013 California Rim Fire: synergistic impacts of reactive hydrocarbons and enhanced oxidants,  
1139 *Atmos. Chem. Phys.*, 22, 4253–4275, <https://doi.org/10.5194/acp-22-4253-2022>, 2022.
- 1140 Wu, Y., Zhao, K., Ren, X., Dickerson, R. R., Huang, J., Schwab, M. J., Stratton, P. R., Daley, H., Li, D.,  
1141 and Moshary, F.: Ozone pollution episodes and PBL height variation in the NYC urban and coastal  
1142 areas during LISTOS 2019, *Atmos. Environ.*, 320, 120317,  
1143 <https://doi.org/10.1016/j.atmosenv.2023.120317>, 2024.
- 1144 Xu, W., Zhang, G., Wang, Y., Tong, S., Zhang, W., Ma, Z., Lin, W., Kuang, Y., Yin, L., and Xu, X.:  
1145 Aerosol Promotes Peroxyacetyl Nitrate Formation During Winter in the North China Plain, *Environ.*  
1146 *Sci. Technol.*, 55, 3568–3581, <https://doi.org/10.1021/acs.est.0c08157>, 2021.
- 1147 Yousefian, F., Faridi, S., Azimi, F., Aghaei, M., Shamsipour, M., Yaghmaeian, K., and Hassanvand, M. S.:  
1148 Temporal variations of ambient air pollutants and meteorological influences on their concentrations in  
1149 Tehran during 2012–2017, *Sci. Rep.*, 10, 292, <https://doi.org/10.1038/s41598-019-56578-6>, 2020.
- 1150 Zara, M., Boersma, K. F., Eskes, H., Denier van der Gon, H., Vilà-Guerau de Arellano, J., Krol, M., van  
1151 der Swaluw, E., Schuch, W., and Velders, G. J. M.: Reductions in nitrogen oxides over the  
1152 Netherlands between 2005 and 2018 observed from space and on the ground: Decreasing emissions  
1153 and increasing O<sub>3</sub> indicate changing NO<sub>x</sub> chemistry, *Atmos. Environ.*: X, 9, 100104,  
1154 <https://doi.org/10.1016/j.aeaoa.2021.100104>, 2021.
- 1155 Zhang, J., Wang, T., Chameides, W. L., Cardelino, C., Kwok, J., Blake, D. R., Ding, A., and So, K. L.:  
1156 Ozone production and hydrocarbon reactivity in Hong Kong, Southern China, *Atmos. Chem. Phys.*, 7,  
1157 557–573, <https://doi.org/10.5194/acp-7-557-2007>, 2007.